



# Mechatronics System Design: Analysis and Control – Solar Tracker

MECN4029A – Mechatronics II Assignment

## Group - 22

Sibusiso Sithole	1424744
Kabelo Moshoma	1346560
Sohil Sugreem	845552
Tshepiso Ngwato	841628

Lecturer: Dr. A. Panday

A Mechatronics II report submitted to the Faculty of Engineering and the Built Environment, University of the Witwatersrand, Johannesburg, in partial fulfilment of the requirements for the degree of Bachelor of Science in Engineering (Mechanical).

Johannesburg, May 2024

# CONTENTS

<b>LIST OF FIGURES .....</b>	<b>5</b>
<b>LIST OF TABLES.....</b>	<b>7</b>
<b>1. INTRODUCTION .....</b>	<b>8</b>
<b>1.1. Background .....</b>	<b>8</b>
1.1.1. Solar Tracking.....	8
<b>1.2. Motivation .....</b>	<b>10</b>
1.2.1. Target location .....	10
1.2.2. Feasibility of Solar Panels at Target Location .....	11
1.2.3. Sun's path for target Location.....	11
<b>2. MODELLING.....</b>	<b>13</b>
<b>2.1. System Parameters .....</b>	<b>13</b>
<b>2.2. Physical Model .....</b>	<b>14</b>
<b>2.3. Mathematical Model.....</b>	<b>14</b>
2.3.1. DC motor's Armature circuit .....	15
2.3.2. Motor Load .....	16
2.3.3. Motor armature and Motor load .....	16
2.3.4. Motor plus gear system.....	17
2.3.5. Photovoltaic panel as Load.....	17
2.3.6. Sensor sub-system modelling .....	19
2.3.7. System Block Diagram.....	20
2.3.8. Equivalent system.....	20
<b>2.4. Linearize Plant Model.....</b>	<b>20</b>
<b>3. SYSTEM ANALYSIS .....</b>	<b>23</b>
<b>3.1. Uncontrolled system in Time-Domain .....</b>	<b>23</b>
3.1.1. Response of Step Input .....	23
3.1.2. Response of Ramp Input.....	24
3.1.3. Response of Sine Wave Input .....	25
3.1.4. System characteristics for Transfer Function with Unit step input.....	25
<b>3.2. Uncontrolled system in Frequency-Domain .....</b>	<b>28</b>

<b>3.3. Linear vs Non-Linear time responses .....</b>	<b>30</b>
3.3.1. Step Input.....	30
3.3.2. Ramp Input .....	31
3.3.3. Sinusoidal Input.....	31
<b>3.4. Uncontrolled Closed loop Stability Analysis .....</b>	<b>32</b>
3.4.1. Pole-Zero Plot.....	32
3.4.2. Nyquist Plot .....	33
3.4.3. Routh-Hurwitz criterion.....	35
<b>4. CONTROLLER IMPLEMENTATION .....</b>	<b>36</b>
<b>4.1. Root Locus.....</b>	<b>36</b>
<b>4.2. Closed Loop Controller .....</b>	<b>39</b>
4.2.1. P control.....	40
4.2.2. PD control.....	42
4.2.3. PI control .....	43
4.2.4. PID control.....	45
4.2.5. Controller Comparison .....	46
<b>4.3. Evaluating PID Controlled System .....</b>	<b>48</b>
4.3.1. PID Controlled vs Uncontrolled system response .....	48
4.3.2. PID Controlled system stability .....	50
<b>4.4. Controller applied to Solar Data Input.....</b>	<b>53</b>
4.4.1. Controller with Noise and Disturbance .....	54
<b>4.5. Discussion of controller performance .....</b>	<b>56</b>
4.5.1. Control Accuracy and Precision .....	56
4.5.2. Responsiveness.....	56
4.5.3. Stability.....	56
4.5.4. Robustness .....	57
<b>4.6. Discussion of instrumentation needed to fully implement controller .....</b>	<b>57</b>
4.6.1. Micro Controller/ PLC.....	57
4.6.2. Power Supply.....	58
4.6.3. Potentiometer.....	58
4.6.4. DC Motor.....	58
4.6.5. Comparator/Signal Amplifier .....	59
4.6.6. Wi-Fi Module for monitoring .....	59
<b>5. BONUS SECTION .....</b>	Error! Bookmark not defined.
<b>REFERENCES.....</b>	<b>60</b>

<b>APPENDICES .....</b>	<b>63</b>
<b>A.1. MATLAB Codes.....</b>	<b>63</b>
A.1.1. Bode Plot – Uncontrolled .....	63
A.1.2. Bode Plot – PID Controlled.....	63
A.1.3. Nyquist Plot – Uncontrolled.....	63
A.1.4. Nyquist Plot – PID Controlled .....	63
A.1.5. Pole Zero Plot – Uncontrolled.....	64
A.1.6. Pole Zero Plot – PID Controlled .....	64

## LIST OF FIGURES

Figure 1: Possible solar tracking angles [1].....	9
Figure 2: Types of solar tracking [2] .....	9
Figure 3: South-West Engineering building [4].....	10
Figure 4: Annual solar radiation for South Africa [8].....	11
Figure 5: Sun's daily path [9] .....	12
Figure 6: System layout.....	14
Figure 7: Armature-controlled DC motor schematic [10] .....	15
Figure 8: PV panel schematic as actuated by motor .....	18
Figure 9: Tilted solid cuboid schematic [11] .....	18
Figure 10: System block diagram with the controller not yet incorporated .....	20
Figure 11: Block diagram of equivalent system .....	20
Figure 12: Linearized system using Simulink .....	22
Figure 13: Simulink uncontrolled linear system showing inputs and sinks for processing.....	23
Figure 14: Uncontrolled Step Input and Step Response in t-domain .....	24
Figure 15: Uncontrolled Ramp Input and Ramp Response in t-domain .....	24
Figure 16: Uncontrolled Sine Input and Sine Response in t-domain .....	25
Figure 17: System Performance for Uncontrolled system in the t-domain .....	28
Figure 18: Bode Plot of uncontrolled linear system .....	29
Figure 19: Linear vs non-linear step response.....	30
Figure 20: Linear vs non-linear ramp response .....	31
Figure 21: Linear vs non-linear sine wave response .....	32
Figure 22: Pole-Zero plot of uncontrolled linear closed loop system .....	33
Figure 23: Nyquist plot of uncontrolled linear closed loop system.....	34
Figure 24: Routh-Hurwitz stability analysis.....	35
Figure 25: Block Diagram with Controller Gain.....	36
Figure 26: Analytical Sketch of Root Locus.....	37
Figure 27: Routh-Hurwitz criterion technique .....	38
Figure 28: Simulink Root Locus.....	39
Figure 29: Simulink block diagram with P controller .....	41
Figure 30: System responses with step input, uncontrolled system and P control .....	41
Figure 31: Simulink block diagram with PD Controller .....	42
Figure 32: System responses with step input, uncontrolled system and PD .....	43
Figure 33: Simulink block diagram with PI Controller .....	44
Figure 34: System responses with step input, uncontrolled system and PI.....	44

Figure 35: Simulink block diagram with PID Controller .....	45
Figure 36: System responses with step input, uncontrolled system and PID .....	46
Figure 37: Simulink block diagram for all controllers .....	47
Figure 38: System step responses with different controllers applied .....	47
Figure 39: System ramp response with PID controller applied .....	49
Figure 40: System sinusoidal response with PID controller applied .....	49
Figure 41: System Transfer Function with the PID controller introduced .....	50
Figure 42: Pole-Zero plot of PID controlled system .....	51
Figure 43: Nyquist plot of PID controlled system.....	51
Figure 44: Bode plot of PID controlled system .....	52
Figure 45: Solar Tracker Response to the Sun's Input Angle.....	54
Figure 46: Noise and Disturbance System Block Diagram.....	55
Figure 47: Controller Response with Noise and Disturbance. ....	55
Figure 48: Micro Controller [17].....	57
Figure 49: Potentiometer [18].....	58
Figure 50: Permanent Magnet DC Gear Motor [19] .....	59
Figure 51: Signal Amplifier [20] .....	59
Figure 52: Wi-Fi Module [21] .....	59

## LIST OF TABLES

Table 1: Panel physical parameters.....	13
Table 2: Motor armature sub-system parameters.....	13
Table 3: Motor load (PV panel) sub-system parameters.....	13
Table 4: Uncontrolled system Margins for Bode Plot .....	29
Table 5: Margins for Nyquist plot (similar to those of bode plot for uncontrolled system).....	34
Table 6: Root Locus Specifications .....	39
Table 7: P control parameters .....	40
Table 8: PD control parameters .....	42
Table 9: PI control parameters .....	43
Table 10: PID control parameters .....	45
Table 11: Comparison of controllers.....	46
Table 12: PID controlled margins for Bode Plot .....	52
Table 13: Bode Plot margin comparison.....	52

# 1. INTRODUCTION

## 1.1. Background

As electronic devices undergo daily and rapid advancements in this era of the fourth industrial revolution, the demand for an excess of energy within every country also increases. Furthermore, due to environmental concerns such as global warming and pollution, energy needs must be met without polluting the environment, primarily through the utilization of renewable energy sources such as wind power, hydro-power, geothermal and solar energy.

Solar energy is becoming an increasingly appealing option for regions with an abundance of sunlight. However, the cost of solar panels remains considerable, and the efficiency of converting solar energy into electricity is relatively low and hence a need for enhancing the energy efficiency of solar energy conversion is advocated for.

### 1.1.1. Solar Tracking

One of the rapidly expanding techniques used to enhance the energy efficiency of solar energy conversion into electricity is through solar tracking. There are two main types of solar tracking normally used, these being: single axis and dual-axis tracking. For single axis tracking, only one angle is adjustable with the other remaining fixed, whereas with dual-axis tracking systems, two angles are adjustable such that it is noted as being a two-degree of freedom system. In the dual-axis system, one angle known as the azimuth angle is expressed as a clockwise/ anti-clockwise rotation along the horizontal plane, while another angle referred to as the tilt angle is expressed as a measurement from the direction of the incoming sunray to the panel. Some sources also mention a third angle, the zenith angle, which is measured from the vertical direction [1], the figure below depicts the angles involved in the solar tracking technique.

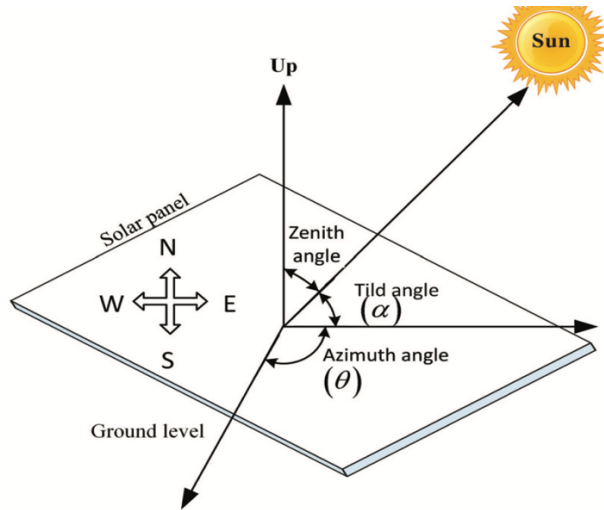


Figure 1: Possible solar tracking angles [1]

It is noted that a properly designed solar tracking system could allow for increase in the output's efficiency up to 40-50% [1], this is because it ensures consistent maximum power output despite fluctuations in solar intensity and environmental temperature. When determining the most effective angle for positioning a solar panel to enhance power generation given the fact that the sun's position is altered throughout the day, implementing a solar tracker emerges as the optimal solution for maximizing energy output.

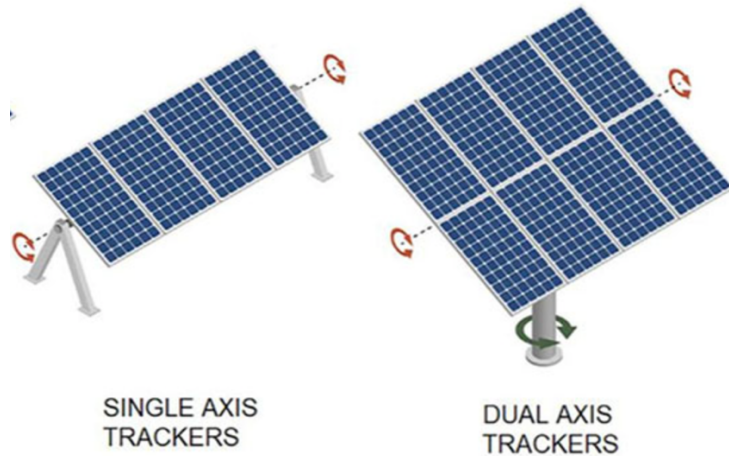


Figure 2: Types of solar tracking [2]

## 1.2. Motivation

### 1.2.1. Target location

The University of the Witwatersrand is currently involved in numerous projects that aim to move the university towards net-zero energy emissions by 2050. Across Wits, there are 14 solar setups aimed at advancing environmental and financial sustainability alongside the hybrid hot water system, this is in alignment with the Wits Sustainability Strategy [3]. These projects are however not inclusive of some buildings and may be considered to not fulfil a sustainable portion of the university's electricity requirements, one such building is the South-West Engineering Building (SWE) which continues to be dependent on diesel generators as a backup power source during loadshedding and outages.



Figure 3: South-West Engineering building [4]

The computers and servers at the SWE PC Pool are required to be operational 24/7 to allow for students and staff to undertake their work at the PC Pools, in their offices or logging in remotely to access required software. The continuous operation of the computers and servers require an uninterrupted supply of electricity and the backup generators used are costly to run especially when considering the high fuel rates in South Africa. A cost effective solution is thus needed which will allow for continuous, uninterrupted operation of the computers and servers in the SWE Building. Furthermore, this is feasible when considering the vast open roof top which will allow for the implementation of a solar power system.

The University of the Witwatersrand has the following coordinates:

- **Latitude:**  $-26^{\circ}11'16.20''$  S [5]

(read as -26 Degrees, 11 minutes and, 16.20 seconds South)

- **Longitude:**  $28^{\circ}01'29.40''$  E [5]

(read as 28 Degrees, 01 minute and, 29.40 seconds East)

### 1.2.2. Feasibility of Solar Panels at Target Location

South Africa boasts some of the most exceptional solar radiation potentials globally, with daily radiation averaging between 4.5 and 7 kWh/m<sup>2</sup> [6]. Typically, South Africa experiences over 2 500 hours of sunlight annually [7], this translates to annual solar radiations between 8 000 and 8 500 MJ/m<sup>2</sup> for Johannesburg, as can be observed in the figure below [8], which highlights the abundant solar resource in the target location.

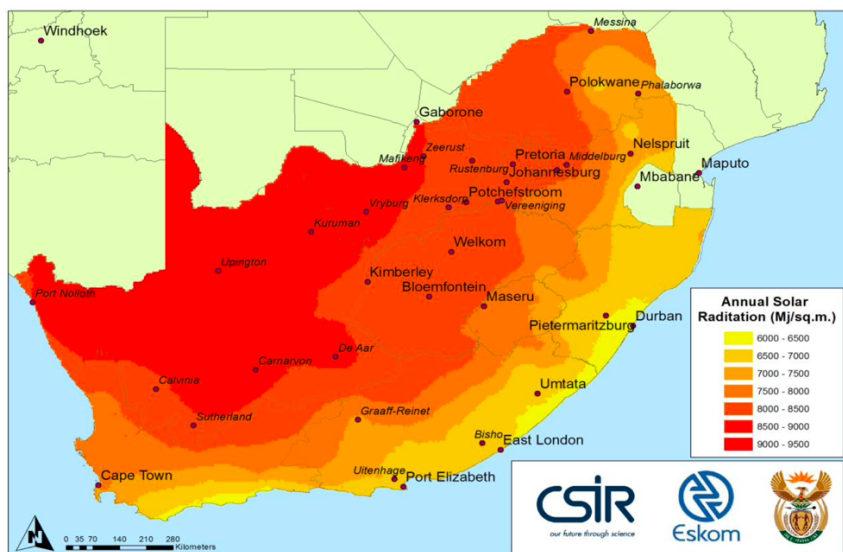


Figure 4: Annual solar radiation for South Africa [8]

### 1.2.3. Sun's path for target Location

In order to design the most efficient solar tracking system, the panels need to be positioned at the most effective yearly angles towards the sun when considering the location's latitude, longitude and climatic conditions. For this to be possible, the annual path of the sun for the target location must be known.

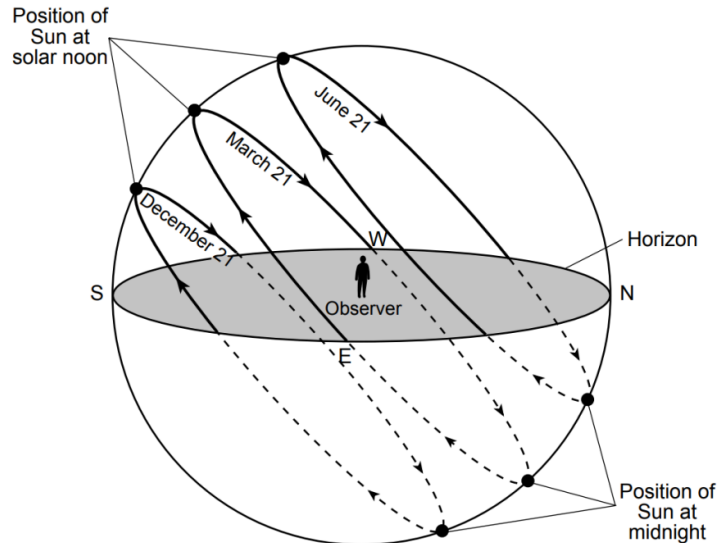


Figure 5: Sun's daily path [9]

From the figure above, the solid lines represent the daytime paths and the dashed lines represent the night time paths as seen by an observer who is located in the Northern Hemisphere. For an observer in the Southern Hemisphere, the 'June 21' and 'December 21' lines are swapped. This explains why in South Africa, the days are longer during Summer as compared to Winter.

For this assignment, the sun's annual position will be programmed into the controller for subsequent positioning, to improve the efficiency of output power.

## 2. MODELLING

The modelling of the solar tracker angles produces the desired exposure to sunlight, which the photovoltaic panel will then utilize to produce electricity, current and voltage. Through mathematical modelling it will be possible to analyse various solar tracker angles and the sunlight exposure for each day throughout the course of the year. The microcontroller will act as the central processing unit for the system. Its primary function will be to regulate the angle of the panel in relation to the sun's rays and to process the feedback data required for additional operations.

### 2.1. System Parameters

The system parameters are outlined in the tables below, these will be used throughout this assignment document.

Table 1: Panel physical parameters

Symbol	Parameter	Value	Unit
M	Mass	30	kg
W	Width	1	m
L	Length	1,5	m
d	Depth	0,05	m
A <sub>Surface</sub>	Area	1,5	m <sup>2</sup>
Beta	Elevation angle	0,785398163	rad

Table 2: Motor armature sub-system parameters

Symbol	Parameter	Value	Unit
J <sub>a</sub>	Inertia (Armature)	0,1	kgm <sup>2</sup>
D <sub>a</sub>	Damping constant (Armature)	0,05	rad/s
L <sub>a</sub>	Armature inductance	0,002	H
R <sub>a</sub>	Armature resistance	5	Ohms
K <sub>t</sub>	Torque constant	0,09	Nm/A
K <sub>b</sub>	Back emf constant	0,085	V/rad/s
K <sub>pos1</sub>	Position sensor 1	0,0667	V/degree
K <sub>pos2</sub>	Position sensor 2	0,0667	V/degree

Table 3: Motor load (PV panel) sub-system parameters

Symbol	Parameter	Value	Unit
$D_L$	Damping constant (Load)	0,75	rad/s
$J_L$	Inertia (Load)	5,315625	$\text{kgm}^2$
$K_r$	Gear ratio	200	-
$J_m$	Equivalent Inertia	212625,1	$\text{kgm}^2$
$D_m$	Equivalent Damping constant	0.8	rad/s

## 2.2. Physical Model

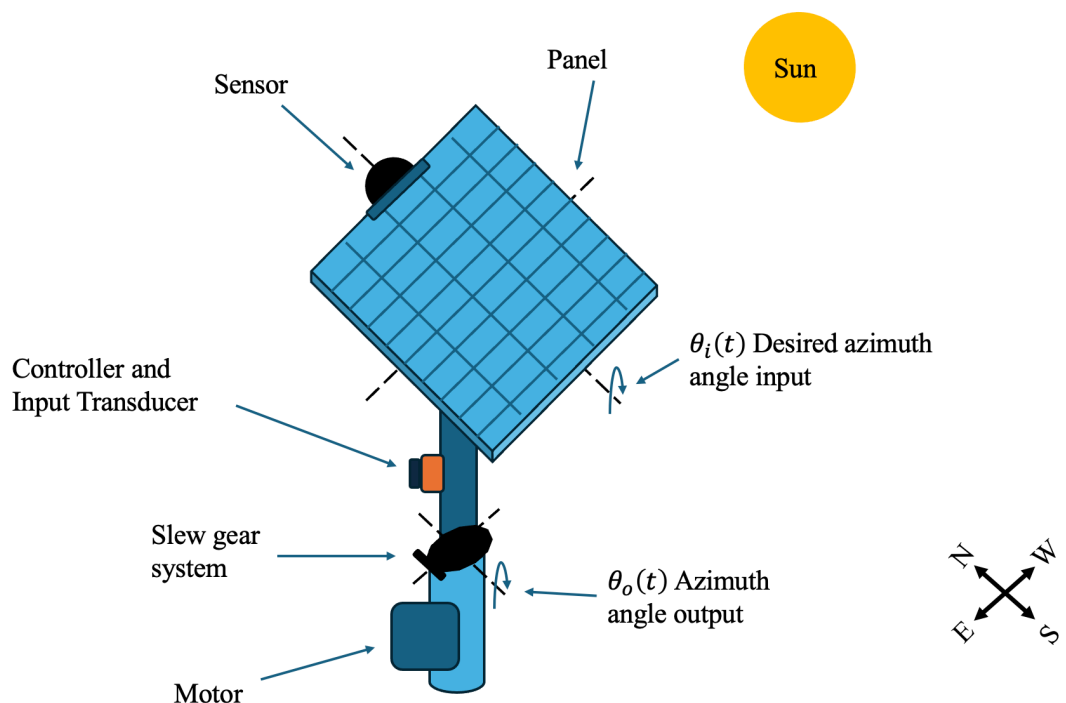


Figure 6: System layout

### Assumptions:

- There are no mechanical or electrical losses in the motor.

## 2.3. Mathematical Model

The mathematical model of the solar tracker is established through fundamental basic laws of physics for both mechanical and electrical systems. Mathematically modelling the solar tracker system entails

representing the DC motor coupled with a load via the use of a slew gear system, such that the load represents the solar panel.

### 2.3.1. DC motor's Armature circuit

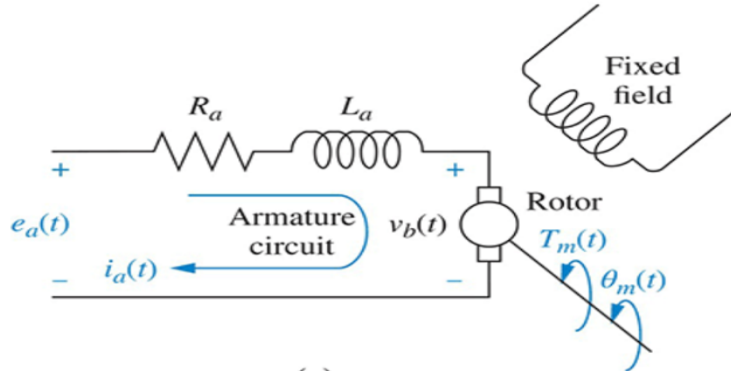


Figure 7: Armature-controlled DC motor schematic [10]

The motor is an electromechanical component which yields a displacement output for a voltage input. The transfer function that represents the motor's sub-system is derived below.

The equation for the armature circuit's back emf is obtained to be.

$$v_b(t) = k_b \dot{\theta}_m(t) \quad (1)$$

Where ' $v_b$ ' is the back emf, ' $k_b$ ' is the back emf constant and ' $\dot{\theta}_m$ ' is the angular velocity of the motor in the Time-domain. Converting the above equation into the s-domain, it's Laplace Transform is obtained.

$$V_b(s) = k_b s \theta_m(s) \quad (2)$$

Using Kirchhoff's Voltage Law (KVL) within the loop in the armature circuit, the following expression is obtained.

$$R_a I_a(s) + L_a s I_a(s) + V_a(s) = E_a(s) \quad (3)$$

Where ' $R_a$ ' is the armature resistance, ' $I_a$ ' is the armature current, ' $L_a$ ' is the armature inductance and ' $E_a$ ' is the armature voltage. Representing the equation above as the armature current and incorporating equation 2, yields the following expression.

$$I_a(s) = \frac{E_a(s) - k_b s \theta_m(s)}{sL_a + R_a} \quad (4)$$

Furthermore, the torque developed by the motor is expressed below, where ' $k_t$ ' is noted to be the torque constant.

$$T_m(s) = k_t I_a(s) \quad (5)$$

### 2.3.2. Motor Load

Considering that the motor torque ' $T_m$ ' is used for driving load against inertial and frictional torque. To account for this loading, the typical equivalent mechanical loading on a motor is derived and converted into the s-domain.

$$T_m(t) = J_m \ddot{\theta}_m(t) + D_m \dot{\theta}_m(t) \quad (6)$$

Converting into the s-domain:

$$T_m(s) = s^2 J_m \theta_m(s) + s D_m \theta_m(s) = [s^2 J_m + s D_m] \theta_m(s) \quad (7)$$

Where ' $J_m$ ' is the equivalent motor inertia and ' $D_m$ ' is the equivalent motor damping. From equation 5, the motor torque term can be written in terms of the armature current as seen in the equation below.

$$I_a(s) = \frac{T_m(s)}{k_t} = \frac{[s^2 J_m + s D_m] \theta_m(s)}{k_t} \quad (8)$$

### 2.3.3. Motor armature and Motor load

Since equation 4 above is equivalent to equation 8, equating the two yields the expression below.

$$\frac{[s^2 J_m + s D_m] \theta_m(s)}{k_t} = \frac{E_a(s) - k_b s \theta_m(s)}{sL_a + R_a} \quad (9)$$

$$(sL_a + R_a)[s^2 J_m + s D_m] \theta_m(s) + k_t k_b s \theta_m(s) = k_t E_a(s) \quad (10)$$

$$\theta_m(s) [(sL_a + R_a)(s^2 J_m + s D_m) + k_t k_b s] = k_t E_a(s) \quad (11)$$

Computing the transfer function therefore leads to the expression below.

$$G_1(s) = \frac{\theta_m(s)}{E_a(s)} = \frac{k_t}{s [(sL_a + R_a)(sJ_m + D_m) + k_t k_b]} \quad (12)$$

It can be further noted that the above transfer function can be expressed in-terms of the damping ratio ‘ $\zeta$ ’ as well as the system’s natural frequency ‘ $\omega_n$ ’, as follows.

$$\frac{\theta_m(s)}{E_a(s)} \equiv \frac{k_t}{s [s^2 + 2\zeta\omega_n s + \omega_n^2]} \quad (13)$$

#### 2.3.4. Motor plus gear system

Considering the use of the slew gear to orchestrate the azimuth angle rotation of the photovoltaic panel from East to West and back, a gear ratio ‘ $k_r$ ’ exists that needs to be incorporated as this will influence the output angular displacement which is what will be experienced by the PV panel.

$$k_r = \frac{N_{worm}}{N_{gear}} \quad (14)$$

Where ‘ $N_{worm}$ ’ represents the number of teeth within the worm (driver) and ‘ $N_{gear}$ ’ represents the number of teeth on the gear / worm wheel which is the element that is driven. The combined motor plus gear system’s transfer function is therefore.

$$G_2(s) = \left( \frac{N_{worm}}{N_{gear}} \right) \cdot \frac{\theta_m(s)}{E_a(s)} = \frac{\theta(s)}{E_a(s)} \quad (15)$$

#### 2.3.5. Photovoltaic panel as Load

To model the motor and load system as an equivalent system at the motor shaft’s angular displacement, ‘ $\theta_m$ ’, excluding the slew gear mechanism, an equivalent system is derived.

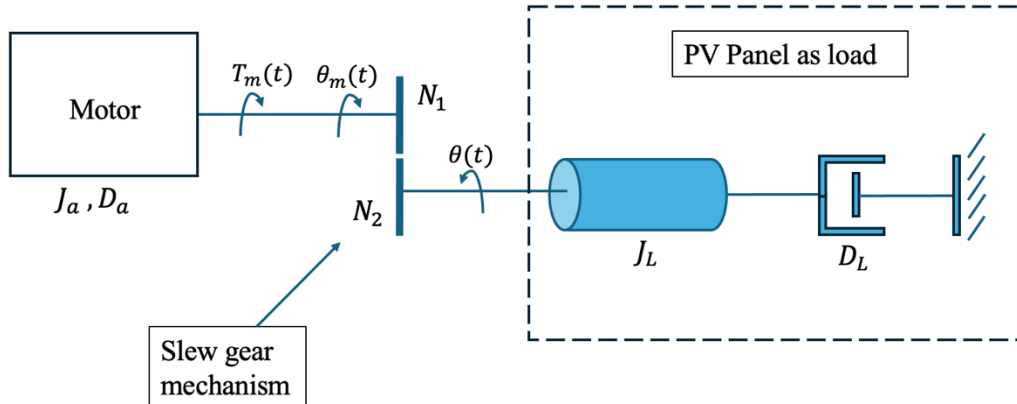


Figure 8: PV panel schematic as actuated by motor

An equivalent system at the input comes from reflecting the gear ratio  $\left(\frac{N_1}{N_2}\right)^2$ , to the rotating body (PV panel) and damper. For the equivalent system,  $J_L$  and  $D_L$  can be reflected back to the armature as some equivalent inertia and damping to be added to  $J_a$  and  $D_a$ , respectively. Thus, the equivalent inertia ' $J_m$ ' and equivalent damping ' $D_m$ ' at the armature can be derived.

$$J_m = J_a + J_L \left(\frac{N_1}{N_2}\right)^2 \quad (16)$$

$$D_m = D_a + D_L \left(\frac{N_1}{N_2}\right)^2 \quad (17)$$

Where ' $J_a$ ' and ' $D_a$ ' represent the armature inertia and armature damping of the motor, respectively and ' $J_L$ ' represents the inertial load, while ' $D_L$ ' represents the damping load of the PV panel.

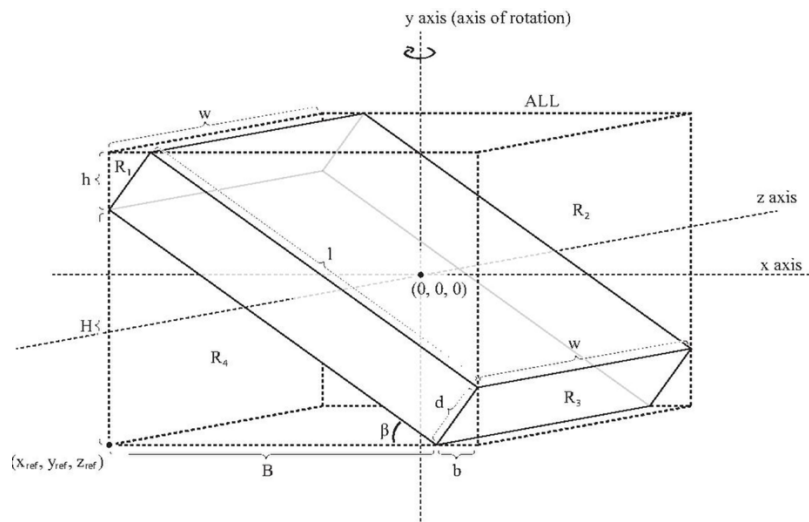


Figure 9: Tilted solid cuboid schematic [11]

The inertia load varies non-linearly as the angles are changed and can be found using the expression below, where ' $d$ ' is the depth of the tilted solid cuboid, ' $w$ ' is its width and ' $l$ ' the length [11].

$$J_L = \frac{m}{12} (l^2 \cos^2 \beta + d^2 \sin^2 \beta + w^2) \quad (18)$$

### 2.3.6. Sensor sub-system modelling

The system will employ a feedback configuration with a potentiometer in the form of a position sensor to ensure that the desired output position is achieved, this is done by determining the location of the solar panel, and therefore preventing it from reaching the edges which would cause it to sustain damage. The potentiometer serves as a sensor to measure the actual output position ' $\theta_o$ ' which is then converted into a corresponding voltage ' $v_o$ '. This voltage value is then fed back into the system.

The output voltage of a potentiometer is expressed as:

$$E_a = \theta_o \times k_{pos2} \quad (19)$$

Where ' $\theta_o$ ' represents the panel's position and ' $k_{pos2}$ ' is the potentiometer constant defined as the ratio of voltage change to the corresponding angle change, which can be written as:

$$k_{pos2} = \frac{\Delta \text{Voltage}}{\Delta \text{Angular Displacement}} \quad (20)$$

Depending on the maximum desired output angle, the appropriate potentiometer can be selected. In this instance the input voltage ' $E_a$ ' ranges from 0 to 12 volts and the angle ranges from 0 to 180 degrees, ' $k_{pos2}$ ' is therefore calculated as follows:

$$k_{pos2} = \frac{12-0}{180-0} = 0.0667 \text{ V/degree} \quad (21)$$

The input potentiometer ' $k_{pos1}$ ' is configured the same way as  $k_{pos2}$ , and is therefore their transfer function will be the same. If these were different, a unit step input would result in a response that does not settle at the same steady-state point, hence  $k_{pos1} = k_{pos2}$ .

### 2.3.7. System Block Diagram

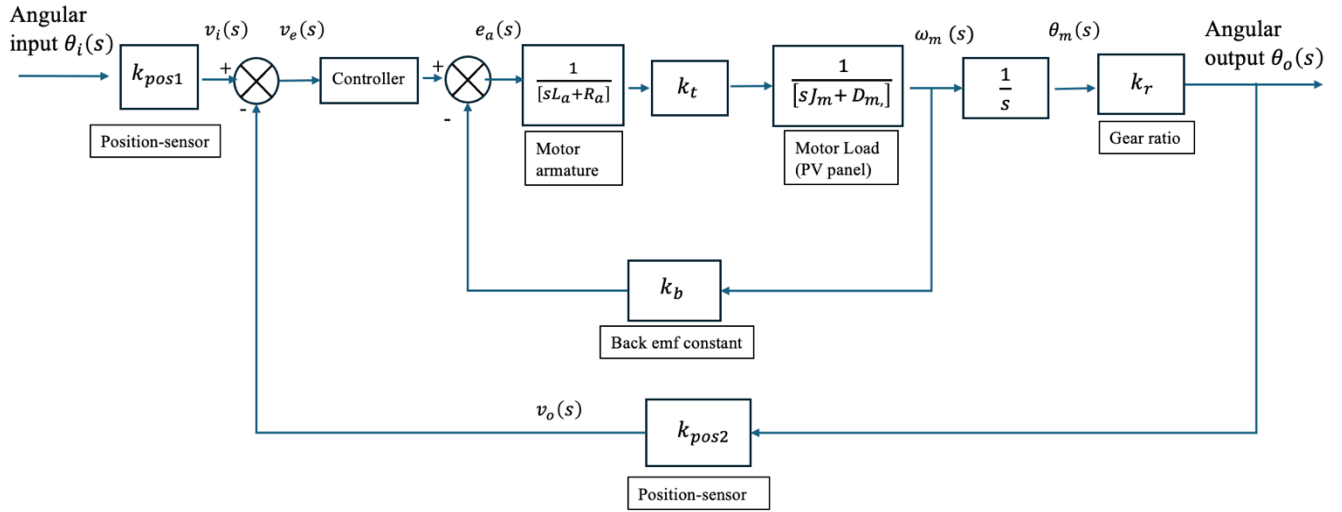


Figure 10: System block diagram with the controller not yet incorporated

### 2.3.8. Equivalent system

Performing block diagram reduction of the system block diagram from Figure 10, by incorporating the various reduction rules such as cascading and loop rule results in the following equivalent system.

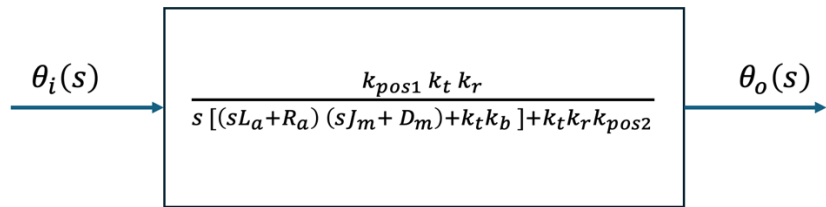


Figure 11: Block diagram of equivalent system

## 2.4. Linearize Plant Model

From the transfer function ' $G(s)$ ', a function 'F' for the Taylor Series can be obtained and the system can be linearized.

$$\theta_i(t) k_{pos1} k_t k_r = L_a J_m \ddot{\theta}_o(t) + L_a D_m \dot{\theta}_o(t) + R_a J_m \ddot{\theta}_o(t) + R_a D_m \dot{\theta}_o(t) + k_t k_b \dot{\theta}_o(t) + k_t k_r k_{pos2} \theta_o(t) \quad (22)$$

$$F[\ddot{\theta}_o, \ddot{\theta}_o, \dot{\theta}_o, \theta_o, \theta_i] = L_a J_m \ddot{\theta}_o(t) + L_a D_m \dot{\theta}_o(t) + R_a J_m \ddot{\theta}_o(t) + R_a D_m \dot{\theta}_o(t) + k_t k_r \theta_o(t) + k_t k_r k_{pos2} \theta_o(t) - \theta_i(t) k_{pos1} k_t k_r = 0 \quad (23)$$

By Taylor Series:

$$f_0 + \frac{\partial F}{\partial \ddot{\theta}_o} \Big|_0 \Delta \ddot{\theta}_o + \frac{\partial F}{\partial \dot{\theta}_o} \Big|_0 \Delta \dot{\theta}_o + \frac{\partial F}{\partial \theta_o} \Big|_0 \Delta \theta_o + \frac{\partial F}{\partial \theta_i} \Big|_0 \Delta \theta_i \quad (24)$$

Where:

$$\Delta \ddot{\theta}_o = (\ddot{\theta}_o - \ddot{\theta}_{o0})$$

$$\Delta \dot{\theta}_o = (\dot{\theta}_o - \dot{\theta}_{o0})$$

$$\Delta \theta_o = (\theta_o - \theta_{o0})$$

$$\Delta \theta_i = (\theta_i - \theta_{i0})$$

System Dynamics:

$$\ddot{\theta}_{o0} = \dot{\theta}_{o0} = \theta_{o0} = 0$$

From eqn. 21 and 22:

$$f_0[\ddot{\theta}_{o0}, \ddot{\theta}_{o0}, \dot{\theta}_{o0}, \theta_{o0}, \theta_{i0}] = k_t k_r k_{pos2} \theta_o - k_{pos1} k_t k_r \theta_i = 0 \quad (25)$$

$$\frac{\partial F}{\partial \ddot{\theta}_o} \Big|_0 \Delta \ddot{\theta}_o = L_a J_m \Delta \ddot{\theta}_o \quad (26)$$

$$\frac{\partial F}{\partial \dot{\theta}_o} \Big|_0 \Delta \dot{\theta}_o = [L_a D_m + R_a J_m] \Delta \dot{\theta}_o \quad (27)$$

$$\frac{\partial F}{\partial \theta_o} \Big|_0 \Delta \theta_o = [R_a D_m + k_t k_b] \Delta \theta_o \quad (28)$$

$$\frac{\partial F}{\partial \theta_i} \Big|_0 \Delta \theta_i = -k_{pos1} k_t k_r \Delta \theta_i \quad (30)$$

$$k_{pos1} k_t k_r \Delta \theta_i = f_0 + L_a J_m \Delta \ddot{\theta}_o + [L_a D_m + R_a J_m] \Delta \dot{\theta}_o + [R_a D_m + k_t k_b] \Delta \theta_o + k_t k_r k_{pos2} \Delta \theta_o$$

$$(0.0667)(0.09)(200)\Delta\theta_i = 0 + (0.002)(5.3156)\Delta\ddot{\theta}_o + [(0.002)(0.8)+(5)(5.3156)]\Delta\ddot{\theta}_o + [(5)(0.8)+(0.09)(0.085)]\Delta\dot{\theta}_o + (0.09)(200)(0.0667)\Delta\theta_o$$

$$(1.2006)\Delta\theta_i = (0.0106312)\Delta\ddot{\theta}_o + (26.5796)\Delta\ddot{\theta}_o + (4.00765)\Delta\dot{\theta}_o + (1.2006)\Delta\theta_o$$

By Laplace, and also dropping ‘ $\Delta$ ’, (assuming zero initial conditions);

$$1.2006 \theta_i = s^3 0.0106312 \theta_o + s^2 26.5796 \theta_o + s 4.00765 \theta_o + 1.2006 \theta_o$$

$$\therefore \frac{\theta_o}{\theta_i} = \frac{112.93}{s^3 + 2500.15 s^2 + 376.97 s + 112.93} \quad (31)$$

The equation above represents the linearized version of our system. Furthermore, using the student package of *Simulink* within ‘MATLAB\_R2024a’, the system was linearized with the aid of the “Model Linearizer” functionality on the software and the result is displayed in the figure below.

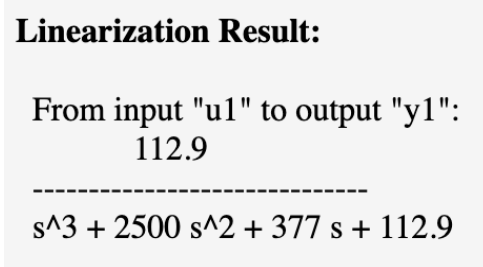


Figure 12: Linearized system using Simulink

The linearization result from the figure above corroborates the mathematically derived linearized model from equation 31.

The overall system’s transfer function ‘ $G(s)$ ’ is therefore computed to be:

$$G(s) = \frac{\theta_o(s)}{\theta_i(s)} = \frac{k_{pos1} k_t k_r}{s [(sL_a + R_a)(sJ_m + D_m) + k_t k_b] + k_t k_r k_{pos2}} \quad (32)$$

### 3. SYSTEM ANALYSIS

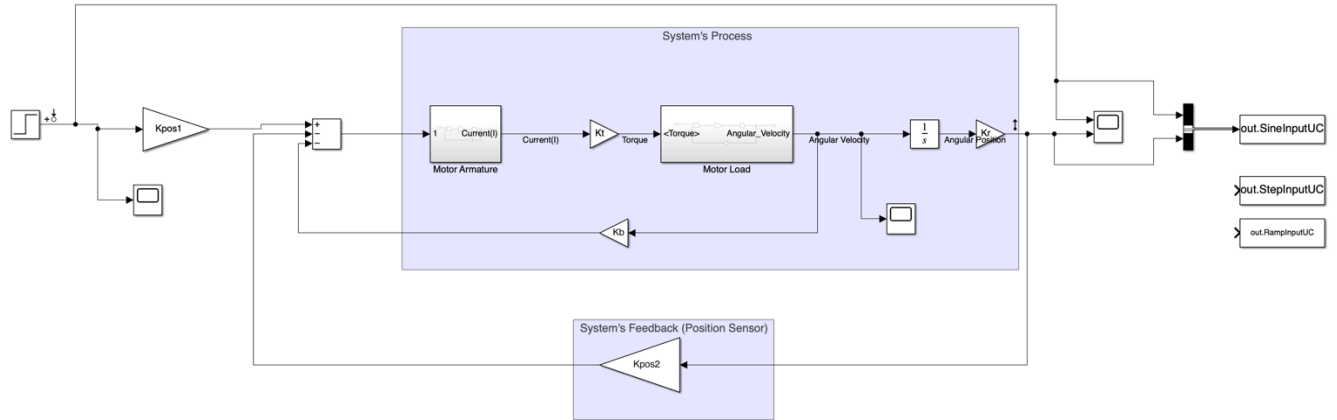


Figure 13: Simulink uncontrolled linear system showing inputs and sinks for processing

#### 3.1. Uncontrolled system in Time-Domain

Using the uncontrolled system in the time-domain within the *Simulink* software, the system was analysed for various inputs to give the step, ramp and sine wave response. The comparisons of the input vs the response are depicted below.

##### 3.1.1. Response of Step Input

The step input is characterised by the sudden change in input which in this context would be attributed to a sudden change in the desired angular displacement. The response exhibits a large overshoot, some oscillations and a slow settling time due to a lack of damping and control. In this case, a controller would aim for a quick adjustment with minimal overshoot and a faster settling time.

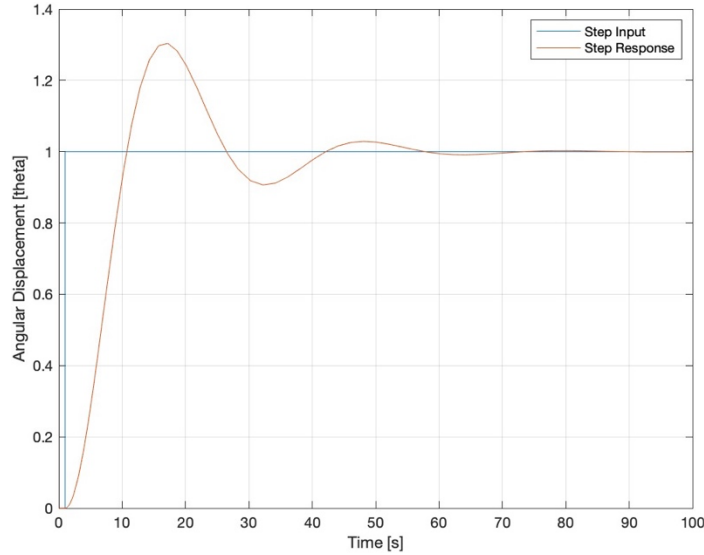


Figure 14: Uncontrolled Step Input and Step Response in t-domain

### 3.1.2. Response of Ramp Input

The ramp input is characterised by a linearly increasing input, which in the application of a solar tracker would simulate a gradual increase in the sun's position over time. From the figure below, it can be noted that the ramp response of the uncontrolled system lags behind the desired angular displacement, unable to keep up with the changing input smoothly and thus resulting in slight periodic errors. It is expected that for such an input, a controller would enable the panel to follow the ramp input closely, therefore maintaining alignment with the sun's position.

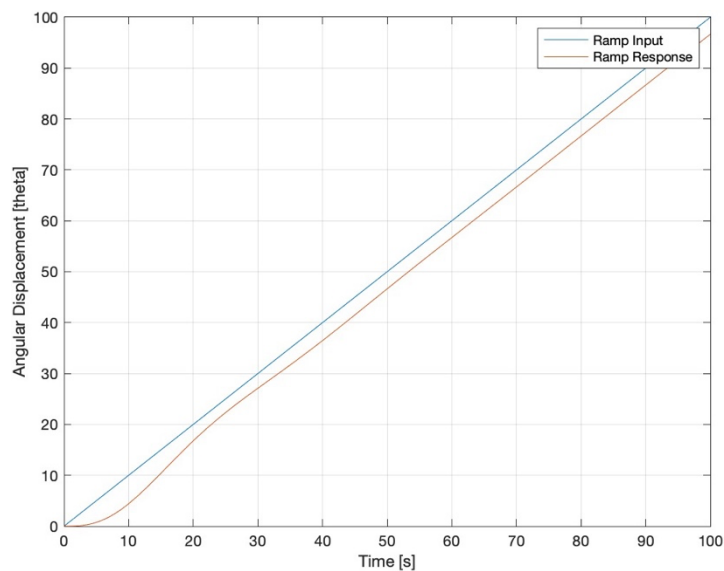


Figure 15: Uncontrolled Ramp Input and Ramp Response in t-domain

### 3.1.3. Response of Sine Wave Input

A sine wave input is characterised by a sinusoidal input, representing oscillatory changes in the sun's position, such as those due to minor movements or reflections. The response of the uncontrolled system is expected to display a phase lag and amplitude errors attributed to the system's inability to accurately follow the oscillations, all this can be observed in the figure below.

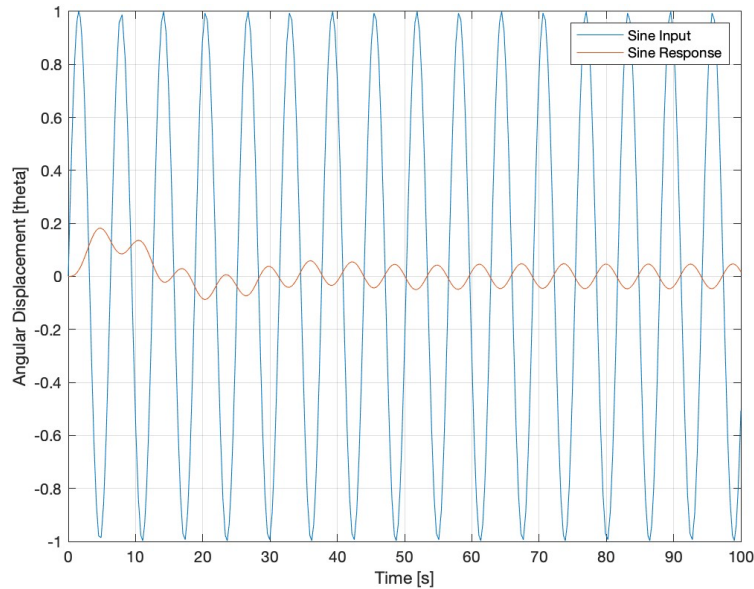


Figure 16: Uncontrolled Sine Input and Sine Response in t-domain

It is worth noting that the deviation between the inputs and responses provide validation for the incorporation of a controller which will lower the deviation by decreasing the effect of the steady-state error on the system's plant.

### 3.1.4. System characteristics for Transfer Function with Unit step input

For the transfer function ' $G(s)$ ', with known poles, characteristics of the system can be evaluated for a transfer function with a unit step input.

$$G(s) = \frac{112.93}{(s+2500)(s^2+0.1508s+0.04517)} \quad (33)$$

For:-

Zeros: 0

Poles:  $s_1 = -2500$ ;  $s_{2,3} = -0.075 \pm j 0.1987$

$-2500 \gg -0.075$  [The real pole is more than 5-times further to the left than the dominant poles]

$\therefore$  The system is replaced by its dominant 2<sup>nd</sup> order pair of poles.

The exponential decay occurs more quickly for ‘pole  $s_1 = -2500$ ’ and therefore, has less effect on the system’s speed of response.

$$\therefore G(s) \approx \frac{112.93}{(s^2 + 0.1508s + 0.04517)} \quad (34)$$

The general 2<sup>nd</sup> order transfer function can therefore be introduced.

$$G(s) = \frac{\omega_n^2}{s^2 + 2\zeta\omega_n s + \omega_n^2} \quad (35)$$

Where, ‘ $\omega_n$ ’ represents the natural frequency and ‘ $\zeta$ ’ is the damping ratio.

$$\omega_n^2 = (0.04517)$$

$$\omega_n = \sqrt{0.04517}$$

$$\therefore \omega_n = 0.21253$$

$$2\zeta\omega_n = 0.1508$$

$$\zeta = \frac{0.1508}{2\omega_n} = \frac{0.1508}{2(0.21253)}$$

$$\therefore \zeta = 0.35477 \text{ (Underdamped)}$$

### 3.1.4.1. Percentage Overshoot:

$$\%OS = e^{-\left(\frac{\zeta\pi}{\sqrt{1-\zeta^2}}\right)} \times 100 = e^{-\left(\frac{(0.35477)\pi}{\sqrt{1-0.35477^2}}\right)} \times 100$$

$$\therefore \%OS = 24.969 \%$$

The plot in the figure below reported a percentage overshoot of 30%, this is close to the one calculated above, which means that assumption made is valid. The slight discrepancy could signify that the fast decaying pole which was ignored, still does have an influence on the system’s transient performance which would contribute to the additional 5% overshoot.

#### 3.1.4.2. Settling Time:

$$\tau_s = \frac{4}{\zeta\omega_n} = \frac{4}{(0.35477)(0.21253)}$$

$$\therefore \tau_s = 54.43 \text{ seconds}$$

The *Simulink* plot generated expressed a settling time of ‘51.5 seconds’ which closely correlates our calculated settling time.

#### 3.1.4.3. Final Value:

The *Simulink* plot depicts a final value of ‘1’, which is expected since this is the steady-state value of a unit step input.

#### 3.1.4.4. Peak Time:

$$\tau_p = \frac{\pi}{\omega_n\sqrt{1-\zeta^2}} = \frac{\pi}{(0.21253)\sqrt{1-(0.35477)^2}}$$

$$\therefore \tau_p = 15.810 \text{ seconds}$$

The *Simulink* plot generated expressed a peak time of ‘15.9 seconds’ which closely correlates our calculated peak time.

#### 3.1.4.5. Rise Time:

$$\tau_r = \omega_n \times \text{Normalized Rise Time} \quad [\text{Assuming a damping ratio of 0.4 since } 0.35477 \approx 0.4]$$

From [12], *Normalized Rise Time* = 1.463

$$\therefore \tau_r = (0.21253)(1.463) = 0.3109 \text{ seconds}$$

It is noted that the calculated rise time and the one generated via *Simulink* are vastly different, this could be attributed to various reasons, such as the fact that the *Simulink* model may include more detailed and realistic components such as damping, and non-linearities due to the panel’s load inertia at the tilt angle is bound to change, which are not accounted for in the mathematical model.

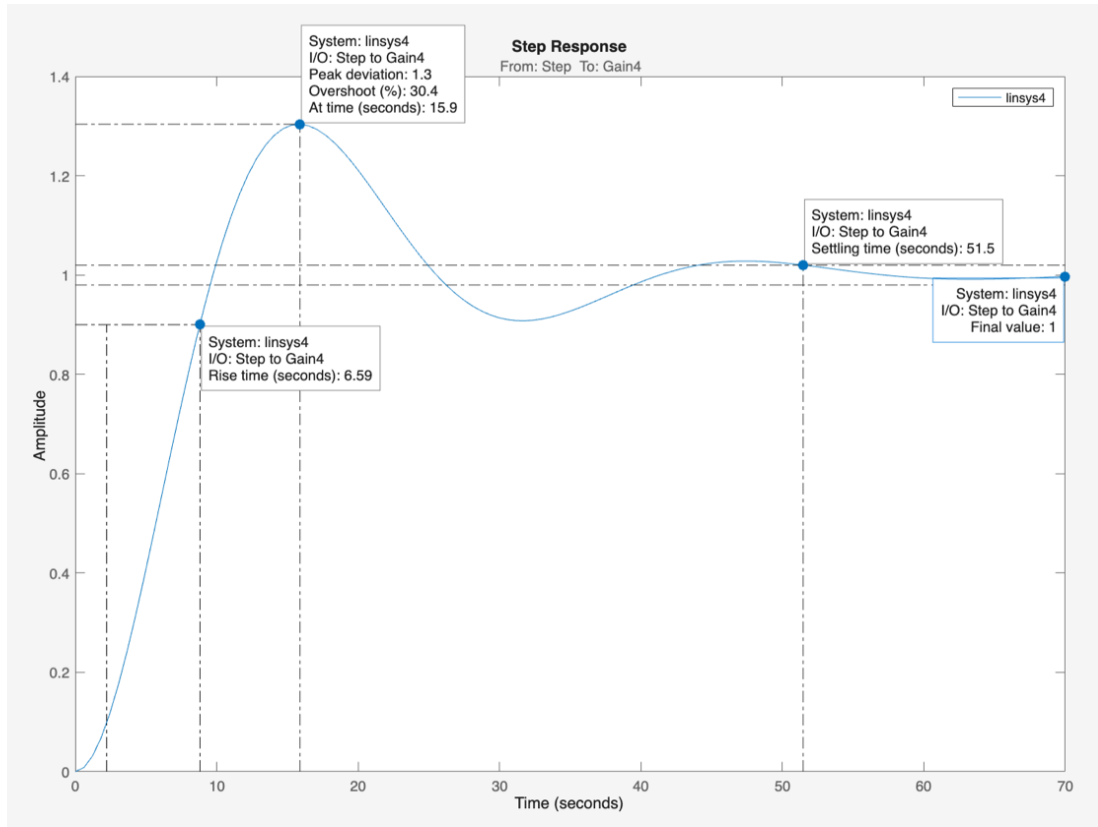


Figure 17: System Performance for Uncontrolled system in the t-domain

Overall, the two methods show very close correlation, signifying the fact that the approximation made in the mathematical expression is also valid to a certain degree.

### 3.2. Uncontrolled system in Frequency-Domain

From the figure below, it is noted from the magnitude plot that at low frequencies, the gain is high, which indicates that the system responds well to slow changes in input, which is expected for a solar tracker considering it needs to follow the relatively slow movement of the sun across the sky. As the frequency increases the magnitude decreases, which suggests that the system is unable to effectively respond to rapid changes in input. However, considering that the sun's motion is gradual, it is unlikely that the solar tracker would need to react/ respond to high frequency inputs.

At a frequency just below 0.26 rad/s, a slight resonant peak can be observed, which indicates a resonant frequency where the system has a tendency to oscillate naturally and can be attributed to the panel's mechanical components which have a natural frequency.

The phase plot starts from zero degrees and begins to lag as the frequency increases indicating that the system has a delay in its response due to input changes.

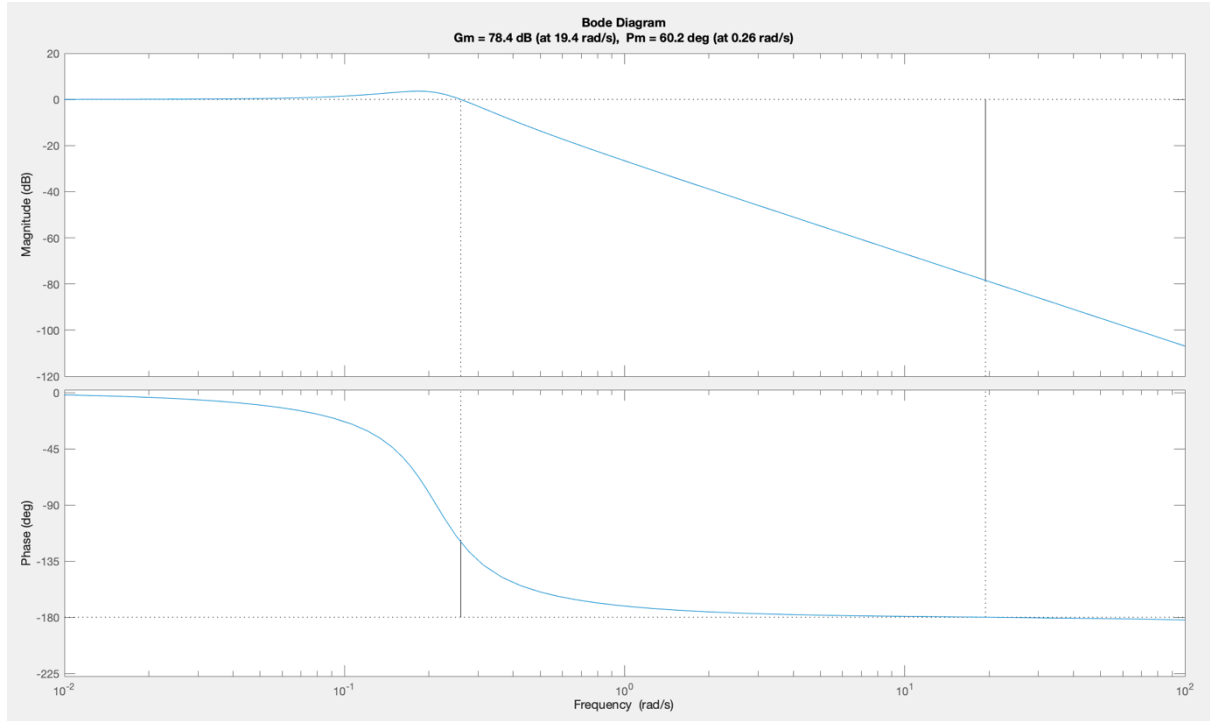


Figure 18: Bode Plot of uncontrolled linear system

Table 4: Uncontrolled system Margins for Bode Plot

Margin type	Margin value	Frequency
Gain	78.4 dB	19.4 rad/s
Phase	60.2 deg	0.26 rad/s

The gain margin shows the extent to which the system gain can be raised before it becomes unstable. A positive gain margin means the system can handle an increase in gain, while the phase margin shows the amount of phase lag that can be added before the system turns unstable. A positive phase margin means the system can withstand some extra phase lag.

### 3.3. Linear vs Non-Linear time responses

The linear and non-linear responses of the system were compared and plotted when different inputs are fed into the system to observe the implications of linearizing a system and noting its deviations from the non-linearized model.

#### 3.3.1. Step Input

A unit step input was fed into the uncontrolled system and plotted against both the linear and non-linear responses to observe the behaviour of angular displacement with increase in time.

From the plot it is observed that the unit step input is represented by a sudden change from 0 to 1 at time equals to zero. The linearized system response also starts from 0 at time equals to zero and its transient section is represented by an exponential rise with a slight overshoot followed by a few oscillations before settling to the final value. During the steady-state, the response eventually settles at the value of 1 (which matches the step input), this is also a hint to us that the system is stable.

The non-linearized response is similar to the linear response, also starting at 0 for time is equal to zero. From the figure below it is observed that this response possesses a more complex behaviour than the linear system, there is a faster rise time and the overshoot is more pronounced, the frequency is also higher as observed by the shorter wavelengths.

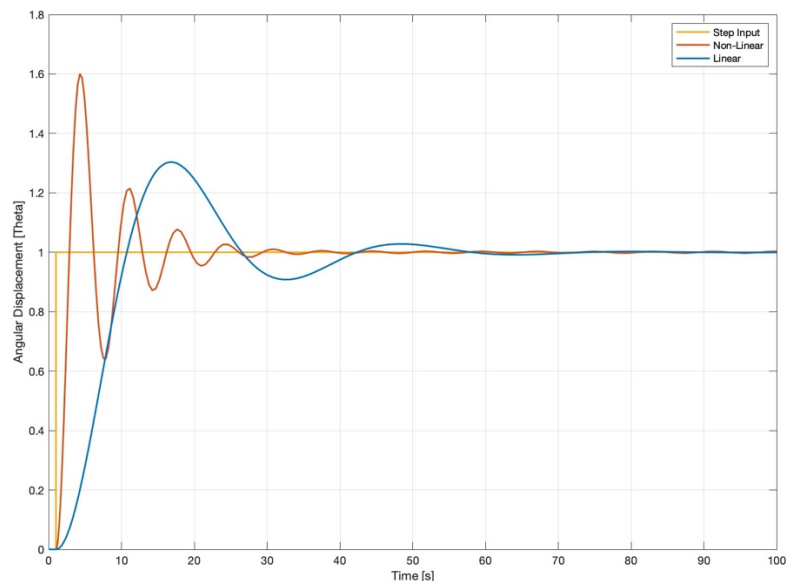


Figure 19: Linear vs non-linear step response

### 3.3.2. Ramp Input

The ramp input increases linearly over time showing a straight line that has a constant positive slope. The linear system response follows the ramp input with some lag which is largely due to the system's time constant. As noted in the figure below, there is an initial delay before the system starts following the ramp input and the constant offset from the ramp input is likely attributed to the steady-state error as there is no controller and thus the system is not able to perfectly follow the increasing input. Interestingly enough, the non-linearized response follows the ramp input quite well and this might be attributed to the fact that the linearities brought about by the inertia of the panel are not that severe, which is expected since the tilt angle does not change (the azimuth angle is being analysed hence tilt angle is kept constant), although there are some deviations at the beginning.

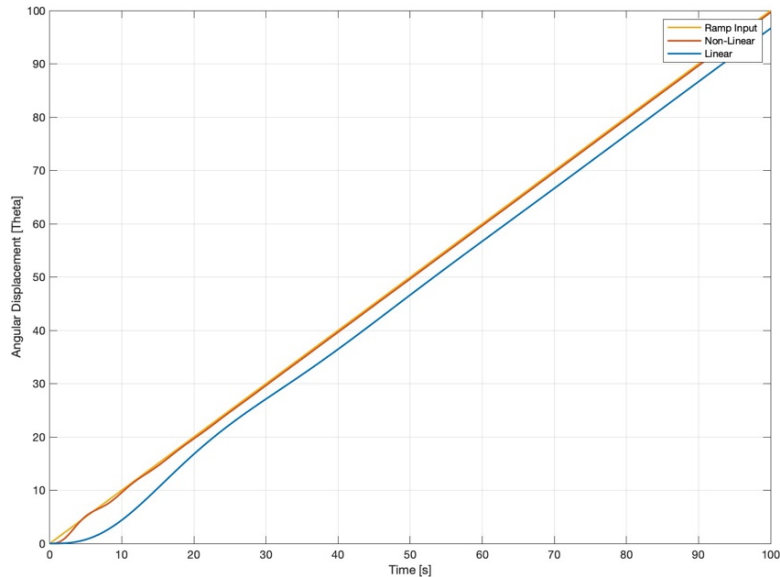


Figure 20: Linear vs non-linear ramp response

### 3.3.3. Sinusoidal Input

The linearized sine wave closely follow the sinusoidal input with both plots having the same frequency, however, it is observed that there is a difference in amplitude and a phase shift. The non-linear displays initial variations in amplitude which are not consistent with a simple scaled version of the sinusoidal input.

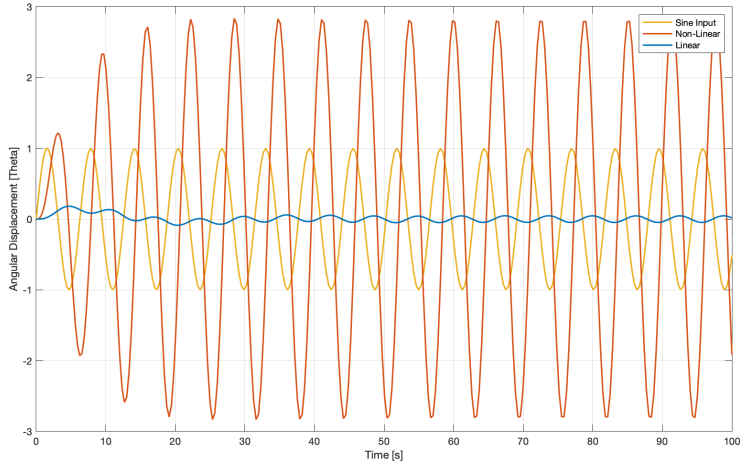


Figure 21: Linear vs non-linear sine wave response

### 3.4. Uncontrolled Closed loop Stability Analysis

#### 3.4.1. Pole-Zero Plot

Using the Zero-Pole Gain method of the system's transfer function from equation 33 the following function is obtained and from it the poles of the system can be obtained. Furthermore, it is observed that there are no zeros in the system's function, only poles.

$$G(s) = \frac{112.93}{(s+2500)(s^2+0.1508s+0.04517)} \quad (36)$$

Where:

Zeros: 0

Poles:  $s_1 = -2500$ ;  $s_{2,3} = -0.075 \pm j 0.1987$

The Pole-Zero Map can therefore be plotted and is depicted in the figure below.

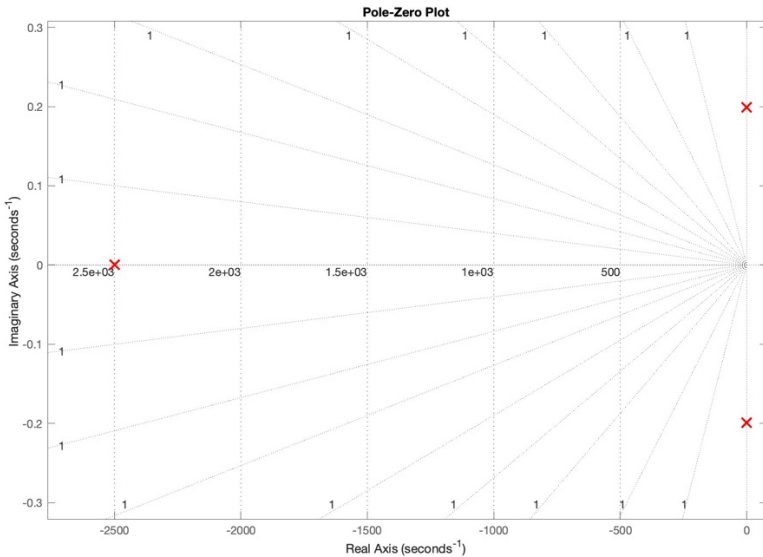


Figure 22: Pole-Zero plot of uncontrolled linear closed loop system

From the Pole-Zero plot is noted that all the poles lie on the Left-Hand side of the s-plane which signify an absolutely stable system.

### 3.4.2. Nyquist Plot

#### 3.4.2.1. Analytical expression for Nyquist plot

From the system's transfer function ' $G(s)$ ', the Nyquist plot can be expressed analytically by letting ' $s = j\omega$ ' and finding the expressions for gain ' $m(\omega)$ ' and phase angle ' $\phi(\omega)$ '.

$$G(j\omega) = \frac{112.9}{(j\omega)^3 + 2500(j\omega)^2 + 377(j\omega) + 112.9} \quad (37)$$

For gain:

$$M(\omega) = |G(j\omega)|$$

Since  $j = \sqrt{-1}$ ,  $j^2 = -1$ ,  $j^3 = -j$

$$M(\omega) = \left| \frac{112.9}{-j\omega^3 - 2500\omega^2 + 377j\omega + 112.9} \right| \quad (38)$$

Grouping real and imaginary terms in the denominator;

$$M(\omega) = \left| \frac{112.9}{(112.9 - 2500\omega^2) + j(377\omega - \omega^3)} \right| \quad (39)$$

$$\therefore m(\omega) = 20 \log(112.9) - 20 \log(\sqrt{(112.9 - 2500\omega^2)^2 + (377\omega - \omega^3)^2}) \quad (40)$$

For the phase angle:

$$\phi(\omega) = \tan^{-1}\left(\frac{0}{112.9}\right) - \tan^{-1}\left(\frac{377\omega - \omega^3}{112.9 - 2500\omega^2}\right) \quad (41)$$

### 3.4.2.2. Numerical method for Nyquist plot

A MATLAB code was developed using the uncontrolled system's transfer function to plot the Nyquist diagram.

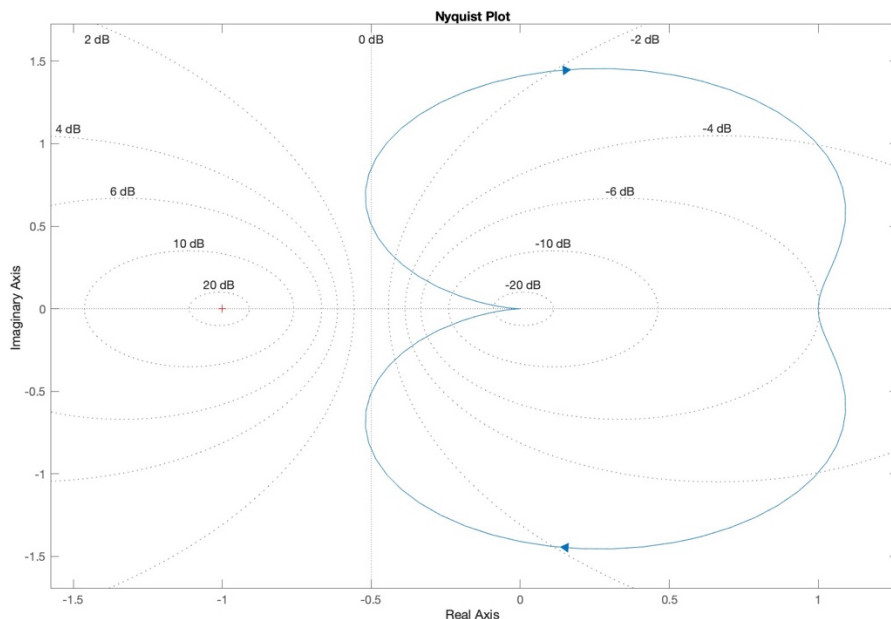


Figure 23: Nyquist plot of uncontrolled linear closed loop system

Table 5: Margins for Nyquist plot (similar to those of bode plot for uncontrolled system)

Margin type	Margin value
Gain	78.4284 dB
Phase	60.2151 deg

The gain margin indicates how much gain can be increased before the system becomes unstable and a gain margin which is greater than 1 suggests a stable system, as is the case here. The phase margin on the other hand indicates how much phase lag can be added before the system becomes unstable, such that a phase margin that is positive indicates a stable system.

### 3.4.3. Routh-Hurwitz criterion

The Routh-Hurwitz criterion is a technique used to provide stability insights without the need to determine the closed loop system poles. Using this approach, we can determine the number of closed-loop system poles located in the left half-plane, the right half-plane, and on the imaginary axis. It is important to note that we identify '*how many poles*', but not their precise locations.

The Routh-Hurwitz criterion states that the number of sign changes in the first column corresponds to the number of roots of the polynomial that lie in the right half-plane. If all the poles of the closed-loop transfer function are located in the left half of the complex plane, the system is considered stable. It can therefore be concluded that the system is stable if there are no sign changes in the first column of the Routh table [13].

$$D(s) = s^3 + 2500 s^2 + 377 s + 112.9$$

$s^3$	1	377
$s^2$	2500	112.9
$s^1$	376.955	0
$s^0$	112.9	0

Figure 24: Routh-Hurwitz stability analysis

Using the Routh-Hurwitz criterion for stability, it can be observed that the uncontrolled linear system is stable, this is noted by the fact that there are no sign changes in the first column meaning that there are no roots in the right half plane, therefore all the roots are on the left half of the complex plane.

## 4. CONTROLLER IMPLEMENTATION

### 4.1. Root Locus

The root locus method is a graphical representation of the poles of a closed loop system as a variable (gain) of the system changes from  $-\infty$  to  $+\infty$ . This method is efficient in describing how the poles of a system are affected by changing a gain of the system. In this instance this method was used to determine the effects of a changing controller proportional gain. This was done to determine for which values is the system stable or unstable. A gain term ( $K_a$ ) was introduced to model the system poles as the controller gain changes.

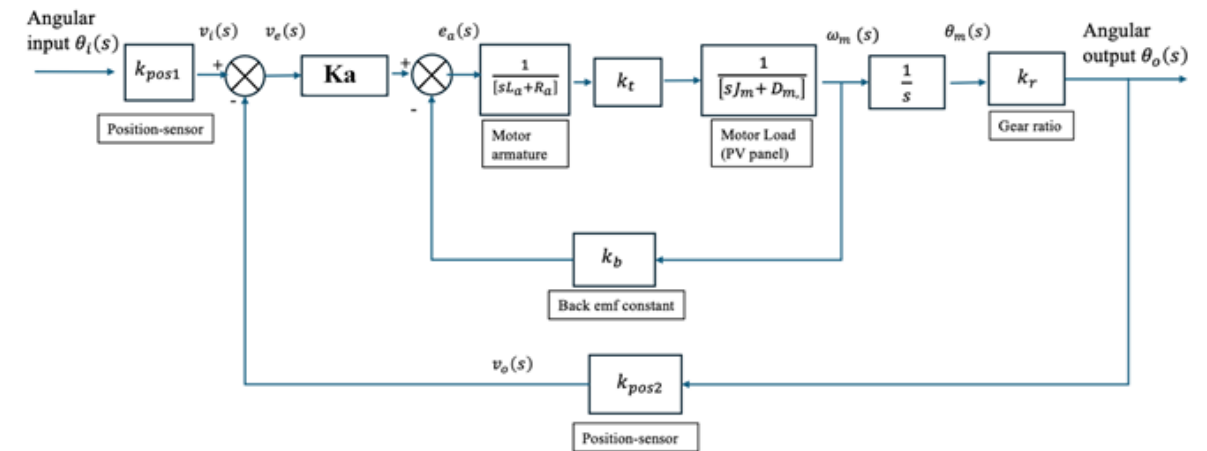


Figure 25: Block Diagram with Controller Gain

Where the open loop transfer function becomes:

$$TF = K_a \left[ \frac{1}{s^3 + 2500s^2 + 377s + 112.9} \right] \quad (42)$$

And the Closed Loop Transfer Function becomes:

$$F(s) = \frac{K_a}{s^3 + 2500s^2 + 377s + 112.9 + K_a} \quad (43)$$

#### 4.1.1.1. Analytical Root Locus

From inspection the open loop transfer function contains 3 finite poles and 0 finite zeros. This means there are 3 infinite zeros. Therefore, analytically it is expected the root locus will have three branches that terminate at  $+\infty$  as the gain increases.

Open loop Poles:  $s = -2500$ ;  $s = -0.08 \pm j0.199$

As there is only one pole on the real axis, one of the branches will exist to the left of ' $s = -2500$ '.

$$\sigma_a = \frac{\sum \text{finite poles} - \sum \text{finite zeros}}{\#\text{finite poles} - \#\text{finite zeros}} \quad (44)$$

$$\theta_a = \frac{(2k+1)\pi}{\#\text{poles} - \#\text{zeros}} \quad \text{for } k = 0, 1, 2 \quad (45)$$

Using equation 44 and 45 the angle of the asymptote and where they intercept the real axis can be determined.  $\theta_a = \frac{\pi}{3}; \pi; \frac{5\pi}{3}$ ,  $\sigma_a = -833.4$

Based on the asymptotes and the open loop poles the root locus does not contain any real axis break-away points.

Therefore, based off the root locus guides the analytical root locus is represented below and will be confirmed using simulation results.

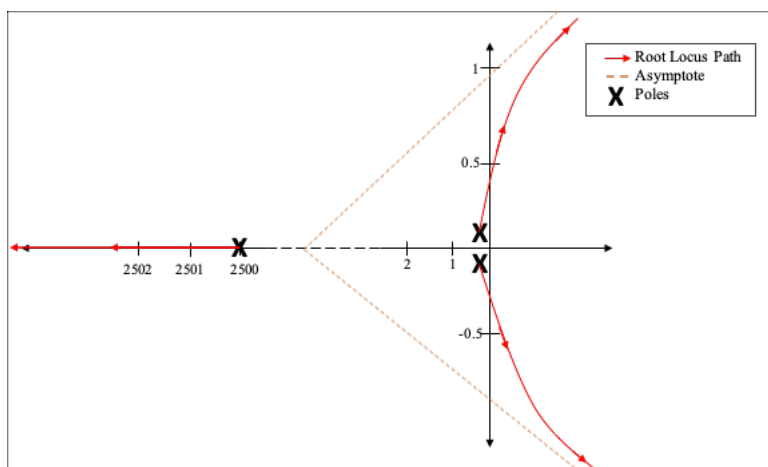


Figure 26: Analytical Sketch of Root Locus

#### 4.1.1.2. $j\omega$ Crossing

The imaginary axis crossing is an important value of the root locus. It determines for which values of  $Ka$  is the system stable. And the oscillation frequency of the system at this critical point. The ' $j\omega$ ' crossing was determined using the Routh Hurwitz criteria [14].

$$D(s) = s^3 + 2500 s^2 + 377 s + 112.9 + Ka$$

$s^3$	1	377
$s^2$	2500	$112.9 + Ka$
$s^1$	$376.955 + \frac{Ka}{2500}$	0
$s^0$	$112.9 + Ka$	0

Figure 27: Routh-Hurwitz criterion technique

According to the Routh Hurwitz criteria, one of the rows must have zeros for the system to have imaginary poles. Therefore  $Ka = 942387.5$  is the maximum gain that can be applied to the system, and it will still be stable. The system will be unstable for  $Ka > 942387.5$ . Using the  $s^2$  row to determine the values of 's' at the imaginary axis crossing ' $s = 19.41j$ '. Therefore, the unstable system will oscillate at a frequency of 19.41 rad/s.

#### 4.1.1.3. Root Locus Simulation

A root locus simulation of the linear system was conducted using *Simulink* and this confirms the analytical computation of the root locus.

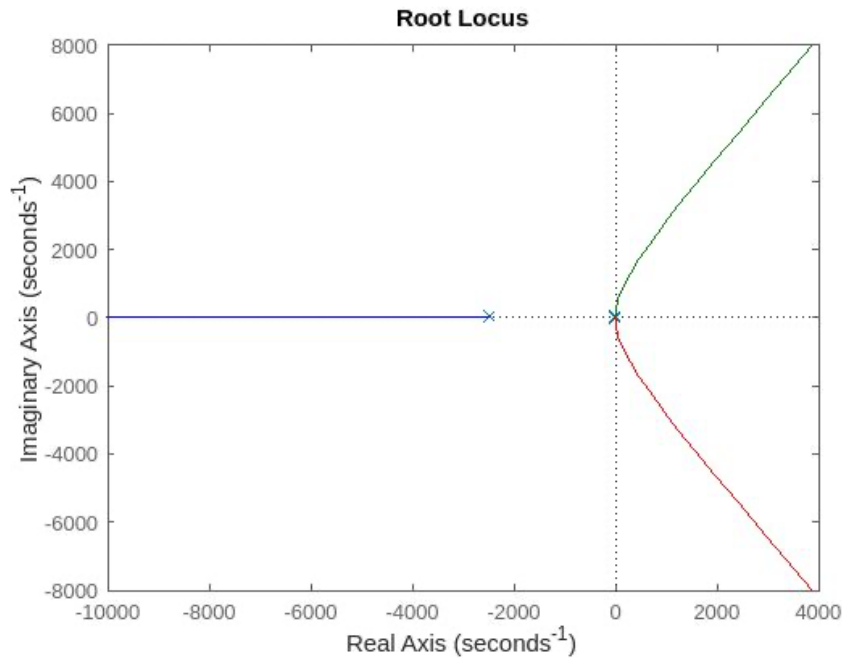


Figure 28: Simulink Root Locus

#### 4.1.1.4. System Specifications Based on Root Locus

Table 6: Root Locus Specifications

Parameter	Outcome
Maximum gain for Stability	942387.5
Frequency of Unstable system	19.416 rad/s
Poles as $K_a \rightarrow \infty$	$\mp \infty$

## 4.2. Closed Loop Controller

To ensure a system operates efficiently, with minimal error and an improved level of stability, a controller is required. A proportional controller ‘P controller’ operates according to the error between the input and output signals meaning that it will control the rotation of the motor shaft until the desired solar panel angle is achieved however it will not be able to hold the solar panel at a specific angle for a period.

Another form of a controller known as a ‘PI controller’ introduces a term with an integral which accounts for previous error signals which is significant in that it will allow the system to always achieve

steady state even after initially not achieving it. In the context of our solar tracker, the PI controller would allow for the motor to continuously rotate the gear system and the solar panel until it achieves the desired position.

A PD controller introduces a derivative term which determines the rate of change of error and adjusts the system accordingly thus making the system more robust. Furthermore, a PID controller consists of both the integral and derivative terms which in most cases proves to be the most effective control method. An analysis on all 4 control methods (P, PD, PI and PID), is conducted below to determine a controller that is the most suitable option for our solar tracker system.

All the controllers analysed below were tuned using the ‘Transfer Function Based – PID Tuner App’ functionality within *Simulink*, and the control parameters tabulated. Furthermore, block diagrams for each controller used are depicted in the subsequent figures below.

#### 4.2.1. P control

A ‘P controller’ modifies the transfer function by introducing a proportional gain ‘ $K_p$ ’, to become;

$$G_P(s) = K_p \times G(s) \quad (46)$$

The denominator polynomial is the same for both the controlled and uncontrolled systems, therefore the location of the poles will not be altered by the introduction of the P controller, therefore the system will still be stable. The tuned ‘ $K_p$ ’ gain can be seen in the table below.

Table 7: P control parameters

P Controller	Value
$K_p$	0.33541

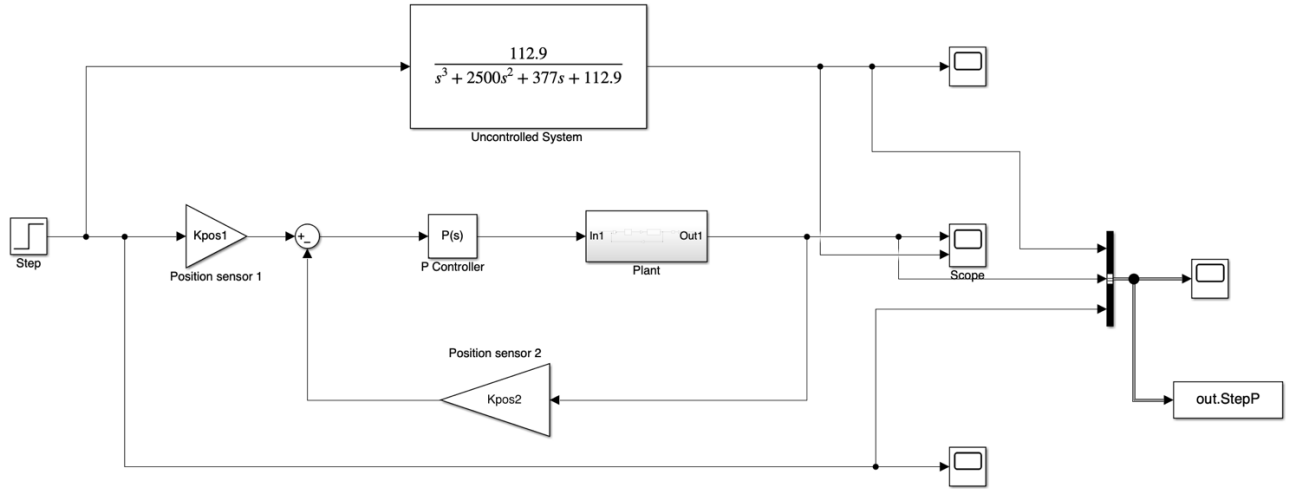


Figure 29: Simulink block diagram with P controller

The figure below displays a plot of the system response when a unit step input is applied to it, both the uncontrolled and P controlled plots can be observed within the same axes.

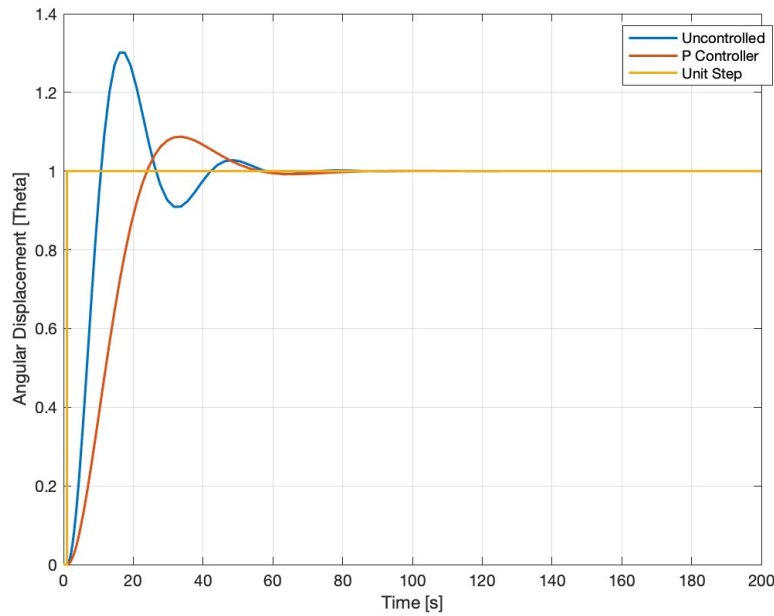


Figure 30: System responses with step input, uncontrolled system and P control

The P controller adjusts the gain and therefore affecting the amplitude, hence from the figure above a lower overshoot can be observed, furthermore, the system's response is much faster with a reduced settling time, which all leads to improved performance.

#### 4.2.2. PD control

The PD controller was introduced to decrease the response time and therefore enable the system to achieve the input's final value much sooner. A PD controller introduces a proportional gain ' $K_p$ ' and a derivative gain ' $K_d$ ', such that the combined transfer function of the system with the PD controller is;

$$G_{PD}(s) = (K_p + K_d s) \times G(s) \quad (47)$$

The tuned gains ' $K_p$ ' and ' $K_d$ ' can be seen in the table below.

Table 8: PD control parameters

PD Controller	Value
$K_p$	1.5621
$K_d$	5.2237

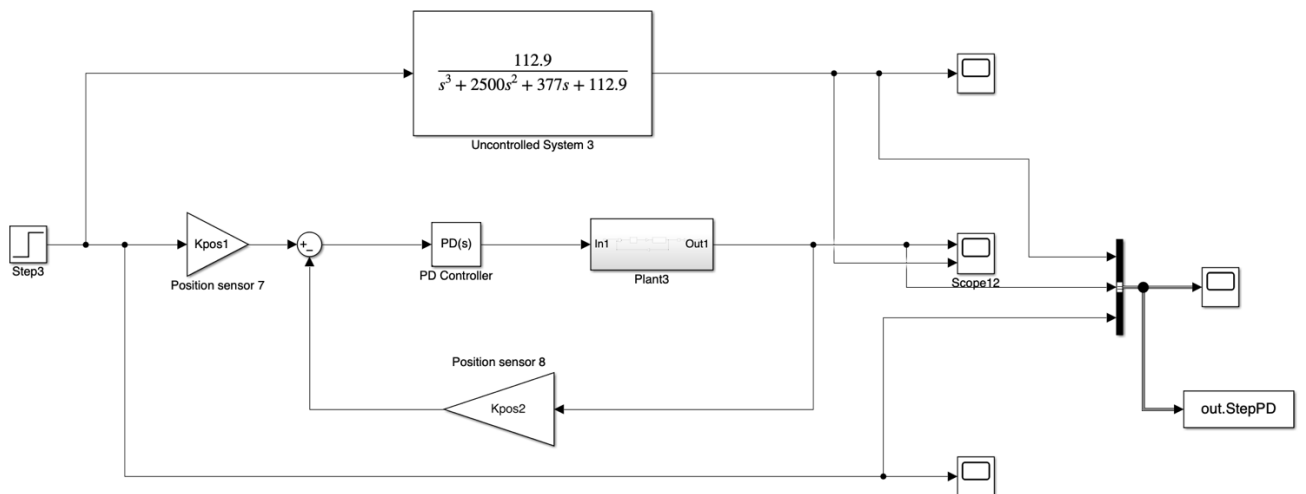


Figure 31: Simulink block diagram with PD Controller

The figure below displays a plot of the system response when a unit step input is applied to it, both the uncontrolled and PD controlled plots can be observed within the same axes.

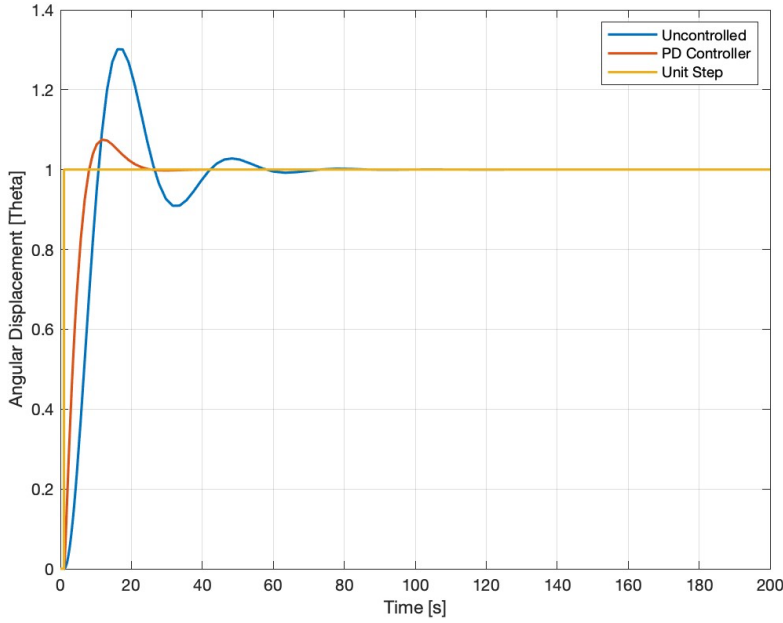


Figure 32: System responses with step input, uncontrolled system and PD

Due to the derivative term that is introduced, the characteristic equation for the controlled system will change and therefore the poles will differ. However, it is observed that all the poles still lie on the left hand side of the s-plane, therefore the system is still stable. Furthermore, from the figure above it can be observed that the controlled system's response is much faster with a reduced settling time as well as a much lower overshoot as compared to the uncontrolled system, this system will therefore have a reduced steady state error.

#### 4.2.3. PI control

The PI controller was tuned to adjust the gains as a way to improve the response time and robustness as a way of lowering the overshoot of the system response. The PI controller introduces a proportional gain ' $K_p$ ' and an integral gain ' $K_i$ ', such that the combine transfer function of the system with the PI controller is;

$$G_{PI}(s) = \left( K_p + \frac{K_i}{s} \right) \times G(s) \quad (48)$$

Table 9: PI control parameters

PI Controller	Value
$K_p$	0.17097
$K_i$	0.0017686

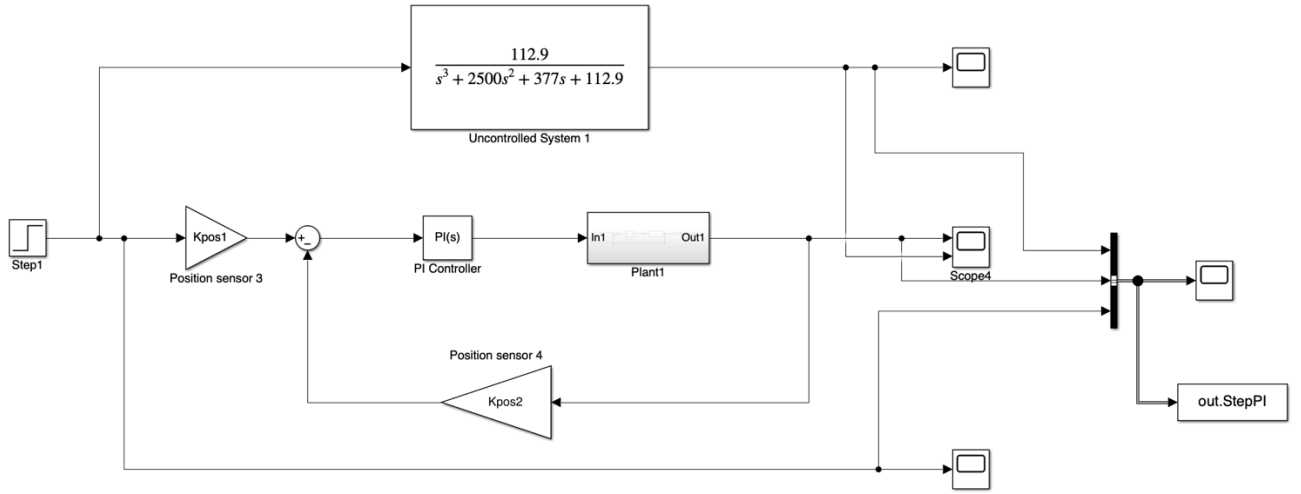


Figure 33: Simulink block diagram with PI Controller

The figure below displays a plot of the system response when a unit step input is applied to it, both the uncontrolled and PI controlled plots can be observed within the same axes.

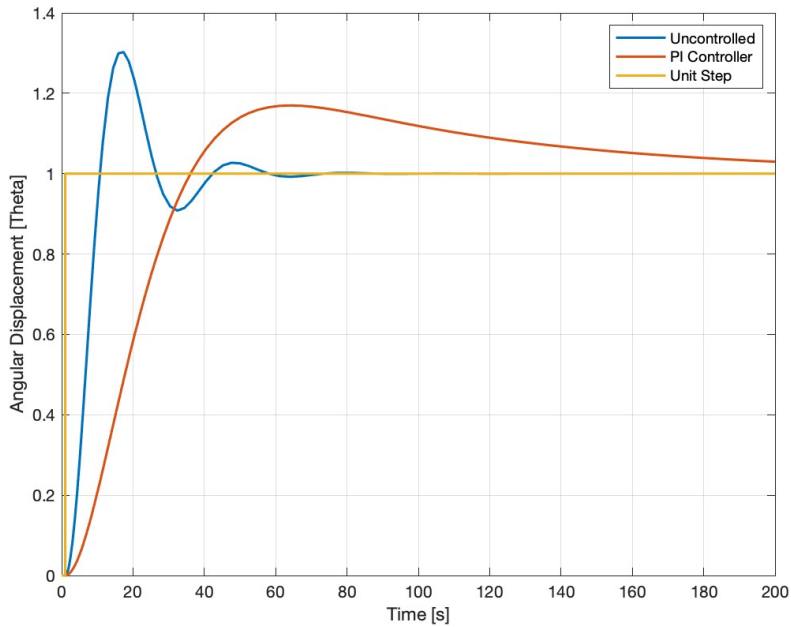


Figure 34: System responses with step input, uncontrolled system and PI

From the figure above it is observed that the PI controlled plant does indeed achieve steady state, however the settling time is much larger than for the uncontrolled plant, which can be attributed to the fact that the PI controller introduces a pole at the origin ( $s = 0$ ) in the closed-loop transfer function, which slows down the transient response because it requires the system to integrate the error over time

to drive it to zero. Therefore since the uncontrolled system already has slow dynamics, the introduction of the integral further slows down the system's response, hence the increased settling time.

#### 4.2.4. PID control

The PID controller incorporate a proportional gain ' $K_p$ ', an integral gain ' $K_i$ ' as well as a derivative gain ' $K_d$ ' such that the combine transfer function of the system with the PI controller is;

$$G_{PID}(s) = \left( K_p + \frac{K_i}{s} + K_d s \right) \times G(s) \quad (49)$$

Considering the integral and derivative gains, the PID controller will add zeros and alter the position of the poles, which would potentially improve the system's overall stability along with its transient response.

Table 10: PID control parameters

PID Controller	Value
$K_p$	3.205
$K_i$	0.17185
$K_d$	14.6946

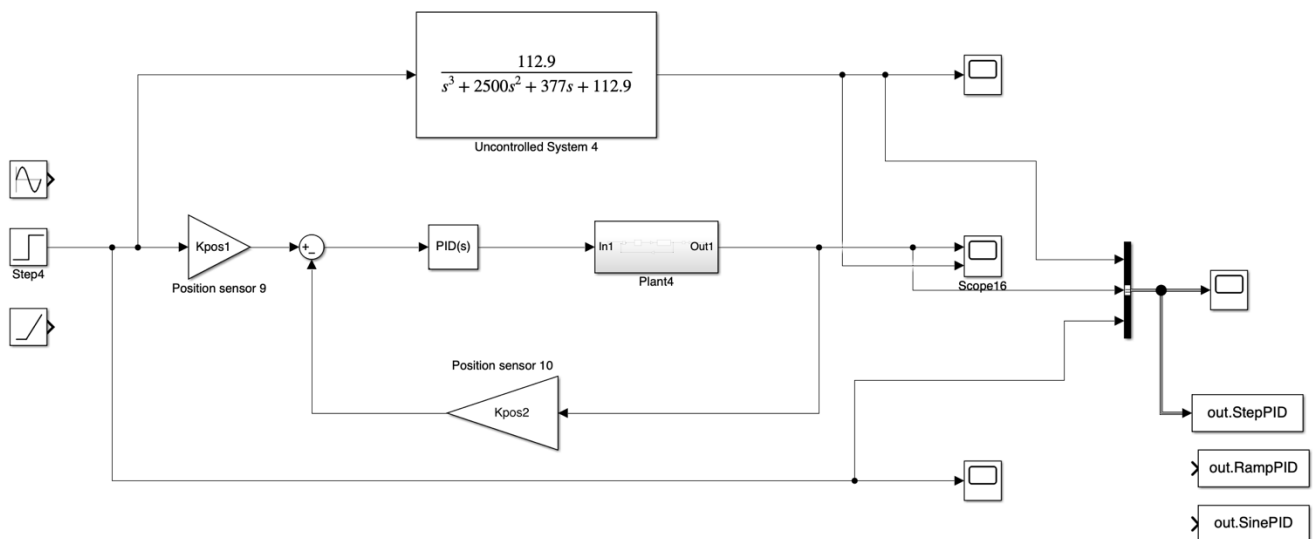


Figure 35: Simulink block diagram with PID Controller

The figure below displays a plot of the system response when a unit step input is applied to it, both the uncontrolled and PID controlled plots can be observed within the same axes.

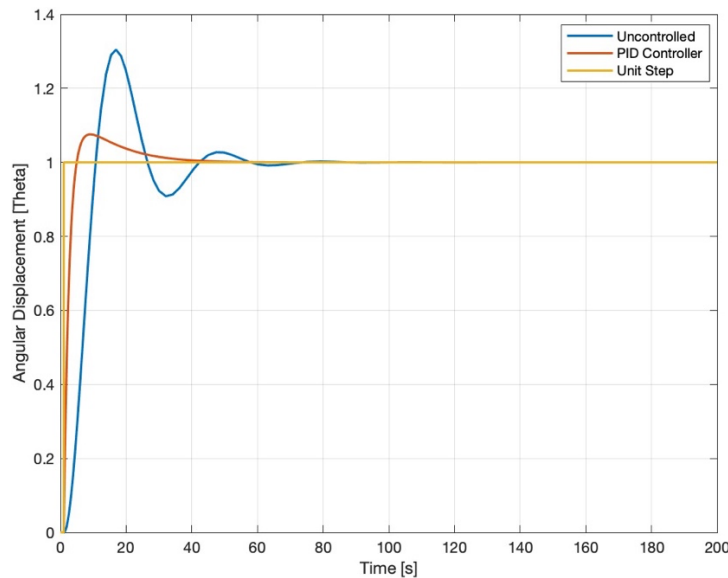


Figure 36: System responses with step input, uncontrolled system and PID

From the figure above it is noted that the rise time is significantly improved, which can be attributed to both the proportional ' $K_p$ ' and derivative ' $K_d$ ' gains, furthermore, there is a reduced settling time which would be attributed to the integral ' $K_i$ ' gain. The reduced overshoot is also noted which is attributed to the combined behaviour of the tuned gains.

#### 4.2.5. Controller Comparison

Table 11: Comparison of controllers

Performance	Controller Type			
	P	PI	PD	PID
Rise Time	15.3 sec.	24.1 sec.	4.96 sec.	2.62 sec.
Settling Time	48.5 sec.	228 sec.	18.9 sec.	25.9 sec.
Overshoot	8.77%	17%	7.63%	7.61%
Peak	1.09	1.17	1.08	1.08

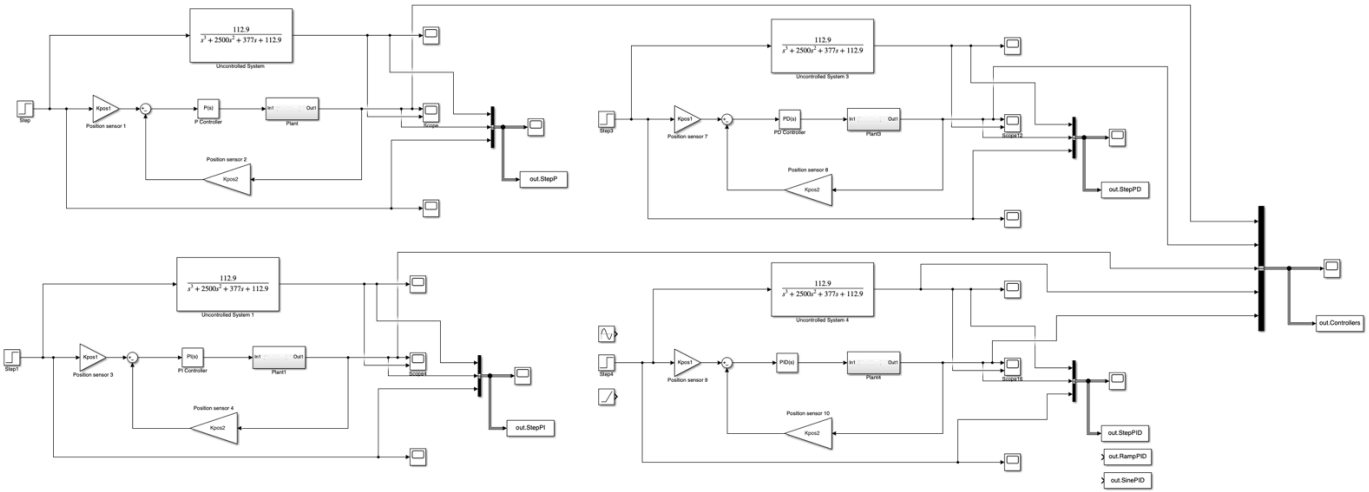


Figure 37: Simulink block diagram for all controllers

The figure below displays a plot of the system responses when a various types of controllers are incorporated.

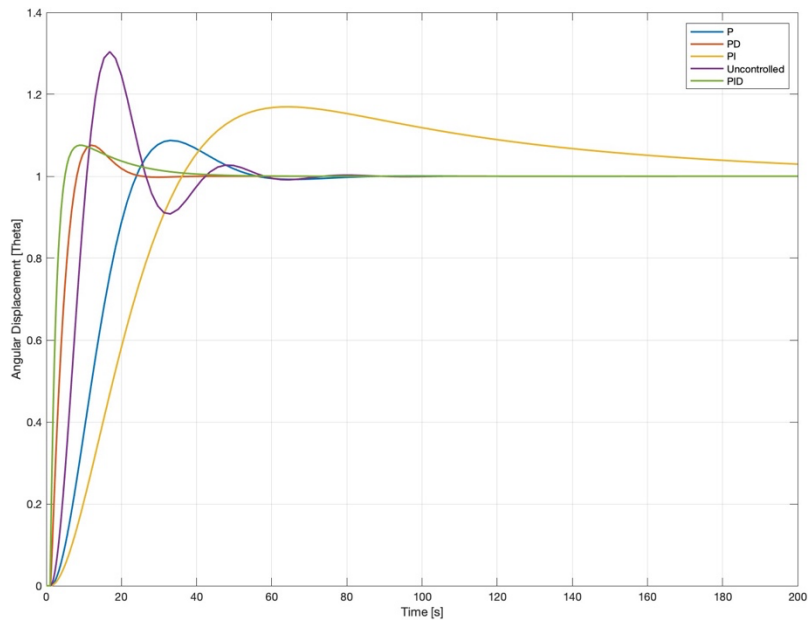


Figure 38: System step responses with different controllers applied

A significant shortfall of the P controller is that it is unable to eliminate the steady-state error and thus leading to a persistent offset. This can be noticed in both the figure and table above by the high settling time of 48.5 seconds because, after the overshoot, the system still oscillates quite a few times before settling, considering that the solar tracker system is not a complex system in terms of its required motion and high precision is not critical, it is not expected that there should be concerns about a significant

steady state error. However, this still does make it a less efficient controller compared to other controllers.

The PD controller shows an improved response time and stability which are observed by the low rise time of 4.96 seconds as well as the lowest settling time amongst all other controllers (18.9 seconds). This maybe largely attributed to the fact that this type of controller considers both the current error and its rate of change. The overshoot of 7.63% is also the second lowest. In comparison with the P controller, the PD controller has better control over oscillations and a much faster response.

Unlike the P controller, the PI controller is able to eliminate the steady state error by integrating the error over time which ensures zero steady state error and thus making it suitable for a solar tracker system since it requires high accuracy in the panel's angle in comparison the sun's angle for improved efficiency. From the table above it is noted that this controller possesses the highest settling time of 228 seconds when compared to other controllers, this is also observable in the figure above as there is a much higher overshoot and the response takes much longer to settle to its steady state value.

The PID controller is observed to combine the benefits of the P, PI and PD controllers which can be noted by its overall superior control ability, this is due to it being able to address the current error, the accumulated error as well as the change of error to minimize the overall transient and steady state errors. Although it can be comparable to the PD controller, the PID controller's rise time of 2.62 seconds as is significant because it entails that this controller is able to ensure optimal performance by balancing speed of response and stability while also providing high accuracy.

### 4.3. Evaluating PID Controlled System

#### 4.3.1. PID Controlled vs Uncontrolled system response

##### 4.3.1.1. Ramp Response

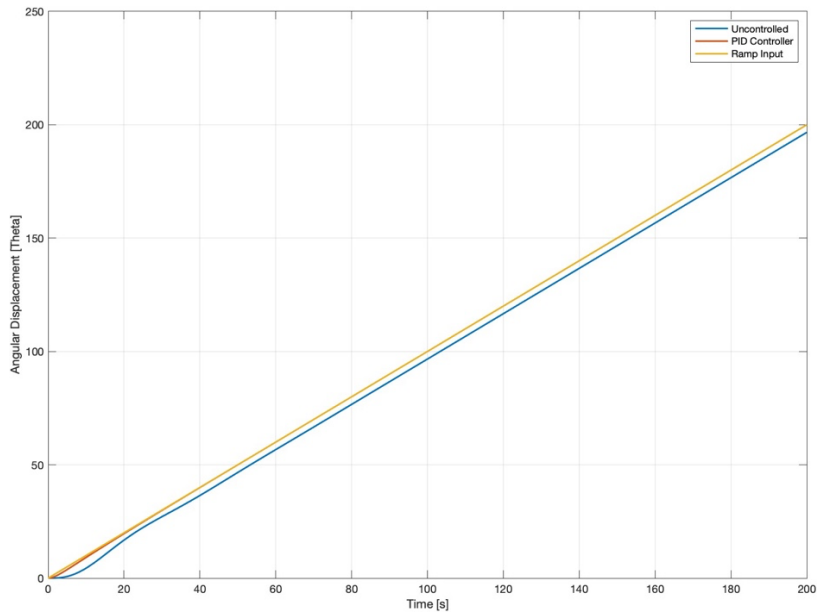


Figure 39: System ramp response with PID controller applied

From the figure above it is noted that the PID controlled ramp response follows the path of the ramp input very closely with only a slight offset within the first 20 seconds. Comparing the response of the uncontrolled and PID controlled system it can easily be concluded that the tuned PID controller works very efficiently and has significantly improved the performance of the system.

#### 4.3.1.2. Sinusoidal Response

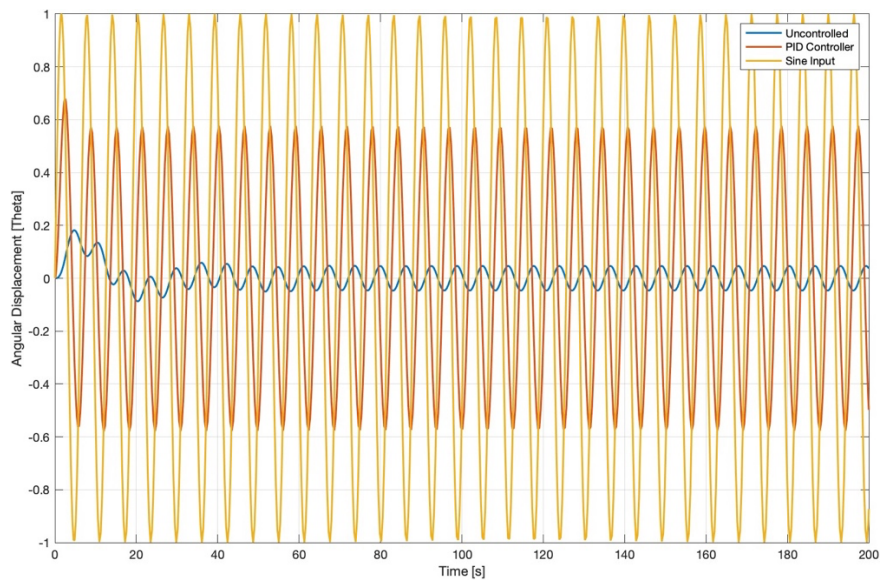


Figure 40: System sinusoidal response with PID controller applied

From the figure above, the PID controlled response is noted to have a frequency that is slightly similar to that of the sinusoidal input, additionally, the amplitude has significantly improved which is slightly half that of the input meaning that the PID controller may need to be further tuned to enhance the system's performance.

The resulting Transfer function with the introduction of the PID controller was evaluated with the aid of *Simulink* to be as displayed in the figure below.

#### Linearization Result:

From input "u1" to output "y1":  

$$1.268e05 s^2 + 2.76e04 s + 1479$$

$$s^5 + 2576 s^4 + 1.909e05 s^3 + 1.556e05 s^2 + 2.76e04 s + 1479$$

Figure 41: System Transfer Function with the PID controller introduced

#### 4.3.2. PID Controlled system stability

##### 4.3.2.1. Pole-Zero Plot – PID controlled system

To provide a visual representation of the poles and zeros for the PID controlled system's transfer function in the complex plane, the Pole-Zero plot was generated.

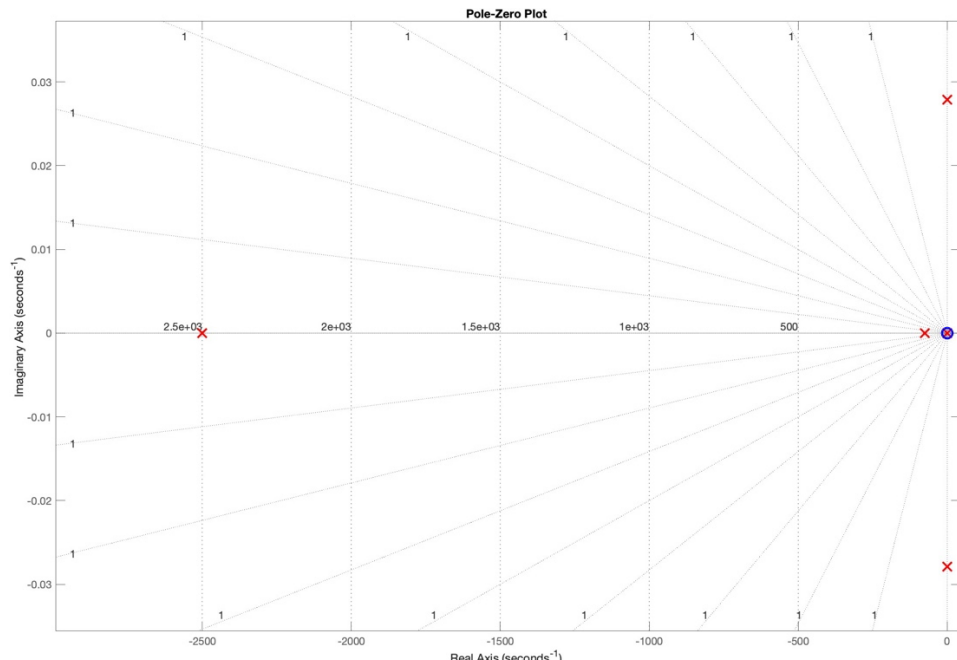


Figure 42: Pole-Zero plot of PID controlled system

When comparing the uncontrolled and PID controlled systems, it is worth noting that the transfer function of the now PID controlled system contains roots in the numerator, and although zeros do not directly affect the stability, they do however influence the response characteristics of the system. The locations of the poles all lie on the left half of the s-plane, which indicate a stable system.

#### 4.3.2.2. Nyquist Plot – PID controlled system

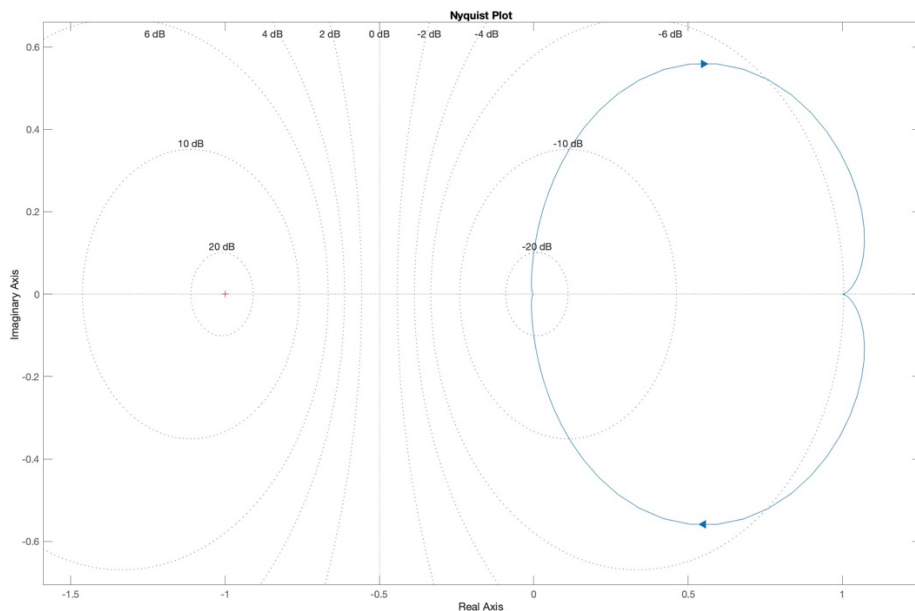


Figure 43: Nyquist plot of PID controlled system

The Nyquist plot is generated to provide insight into the frequency response of the system, especially with regards to the stability margins. For the PID controlled system, the Nyquist plot does not contain any encirclements of the critical point  $-1 + j0$  and there are no right half plane poles, meaning that the system is stable.

#### 4.3.2.3. Bode Plot – PID Controlled system

A Bode Plot for the system with the PID controller introduced was generated using MATLAB and is depicted in the figure below, the code is attached within the appendices.

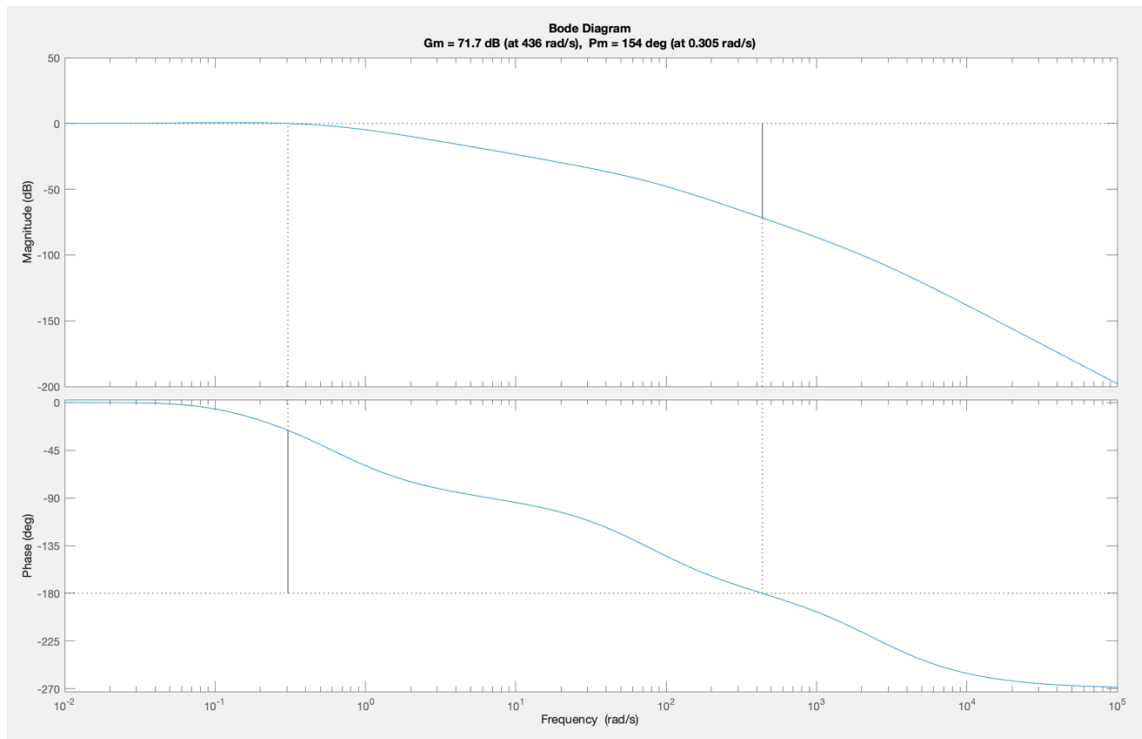


Figure 44: Bode plot of PID controlled system

The margins for the Bode Plot in Figure 44 are tabulated below.

Table 12: PID controlled margins for Bode Plot

Margin type	Margin value	Frequency
Gain	71.7 dB	436 rad/s
Phase	154 deg	0.305 rad/s

#### 4.3.2.4. Controlled vs Uncontrolled Bode Plots

Table 13: Bode Plot margin comparison

Margin type	Uncontrolled		PID Controlled	
	Margin	Frequency	Margin	Frequency
Gain	78.4 dB	19.4 rad/s	71.7 dB	436 rad/s
Phase	60.2 deg	0.26 rad/s	154 deg	0.305 rad/s

Comparing the uncontrolled and PID controlled systems, it is noted that the gain margin has decreased from 78.4 dB to 71.7 dB, and considering that a high gain margin would indicate that the system can tolerate a large increase in gain before becoming unstable, the fact that in this instance the gain margin has decreased indicates that the PID controlled system is slightly less tolerant to gain increases than before. However, 71.7 dB is still a significantly high gain margin, which would suggest that the system still remains robust against variations in gain.

The phase margin on the other hand has increased significantly from 60.2 to 154 degrees, meaning that the system can now tolerate even more phase lag and therefore indicating that the system is now very stable. The introduction of the PID controller has therefore effectively improved the stability and robustness of the solar tracker system.

#### 4.4. Controller applied to Solar Data Input

The solar tracker will receive input from the sun's azimuth angle. The azimuth angle of the sun is similar on a day-to-day basis with only a minor variation of 20 degrees over a season. Thus, the response of the system is computed from the sun's azimuth angle on a summer day. This input was computed from 12 am (midnight) to sunset 6 pm [15]. The azimuth angle of the sun was calculated using equation 50. Where the azimuth angle ' $\theta$ ' is defined in terms of the declination angle ' $\delta$ ' and ' $\alpha$ ', which is the the tilt angle as shown earlier in '**Section 1.1.1**'. The hourly angle ' $h$ ' is defined by equation 52 and is the angle the sun rotates hourly. The sun rotates  $15^\circ$  /hour. The declination angle is the compliment of the zenith angle and is defined by equation 51 where ' $n$ ' is the day number (i.e. the 1<sup>st</sup> of January means that  $n = 1$ ).

$$\sin(\theta) = \frac{\cos(\delta) \sin(h)}{\sin(\alpha)} \quad (50)$$

$$\delta = 23.45^\circ \sin \left[ \frac{360}{365} (n + 284) \right] \quad (51)$$

$$h = \frac{(time - 12)}{15^\circ} \quad (52)$$

$$\sin(\alpha) = \sin(latitude) \cdot \sin(\delta) + \cos(\delta) \cdot \cos(h) \quad (53)$$

Even though the sun is not shining before 6 am in the morning, the input is included to allow the solar tracker to align with the sunrise. The sun rises from an angle of  $73^\circ$  and sets at an angle of  $350^\circ$  [15].

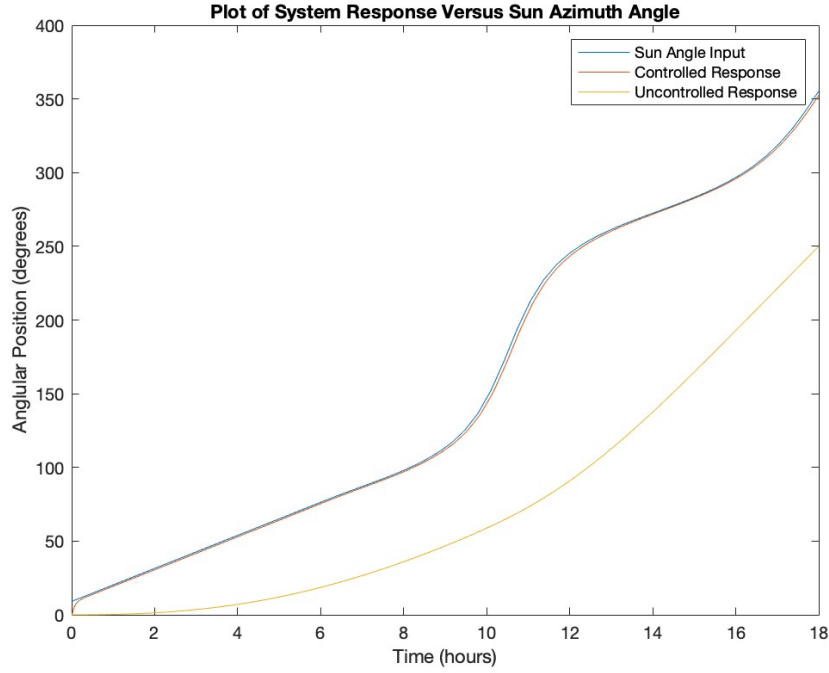


Figure 45: Solar Tracker Response to the Sun's Input Angle.

Figure 45 illustrates that the response of the PID controlled systems allows it to track the angle of the sun accurately without delay or %error, such that it also starts tracking from before 6 am to allow the solar tracker to align with the sun as observed by the controlled plot starting from  $0^\circ$  instead of the sun's  $73^\circ$ . The uncontrolled response depicts that the solar tracker is unable to effectively track the angle of the sun accurately as the % error increases as the day progresses and the angle of the sun increases. This indicates that the uncontrolled system has a response delay. This highlights the significance of implementing a controller into the system and also suggests that our selected PID controller allows for optimal solar tracker performance, furthermore, this performance indicates the type of error a system may output when there is no controller implemented.

#### 4.4.1. Controller with Noise and Disturbance

During operation the solar panel will be subjected to wind loads that will induce a drag force onto the panel. In the control system this is accounted for in the form of a disturbance signal. The disturbance signal was modelled as a random number signal as the wind is unpredictable. Another factor that was considered is noise due to sensors. Sensors such as the potentiometer are prone to noise that may affect the error signal this was accounted for using band limited white noise signal as shown in Figure 46. The value of the disturbance signal was input as a maximum of 4 N and a minimum of 0 N, due to a maximum wind speed of 1,3 m/s [16].

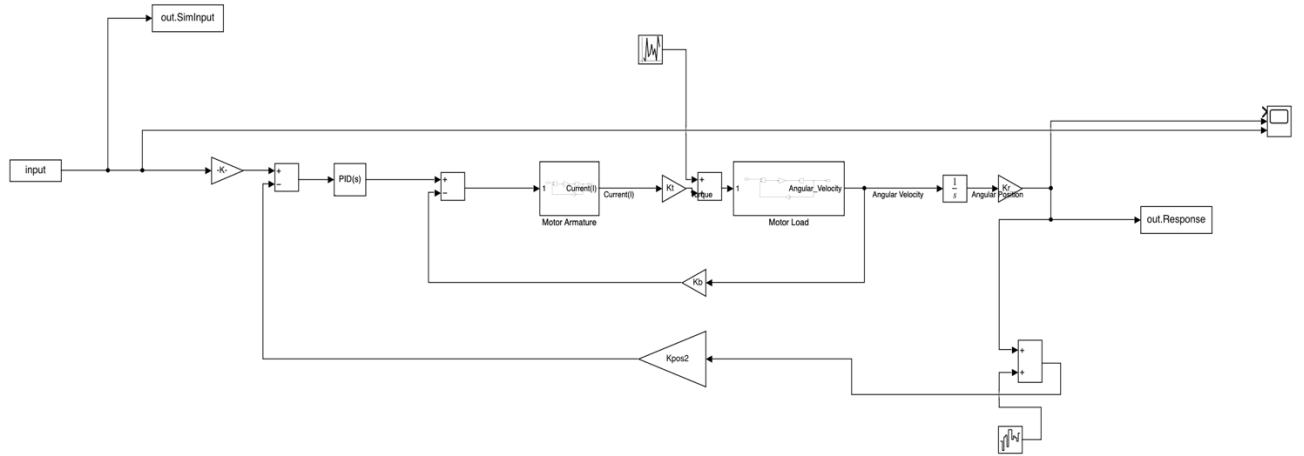


Figure 46: Noise and Disturbance System Block Diagram

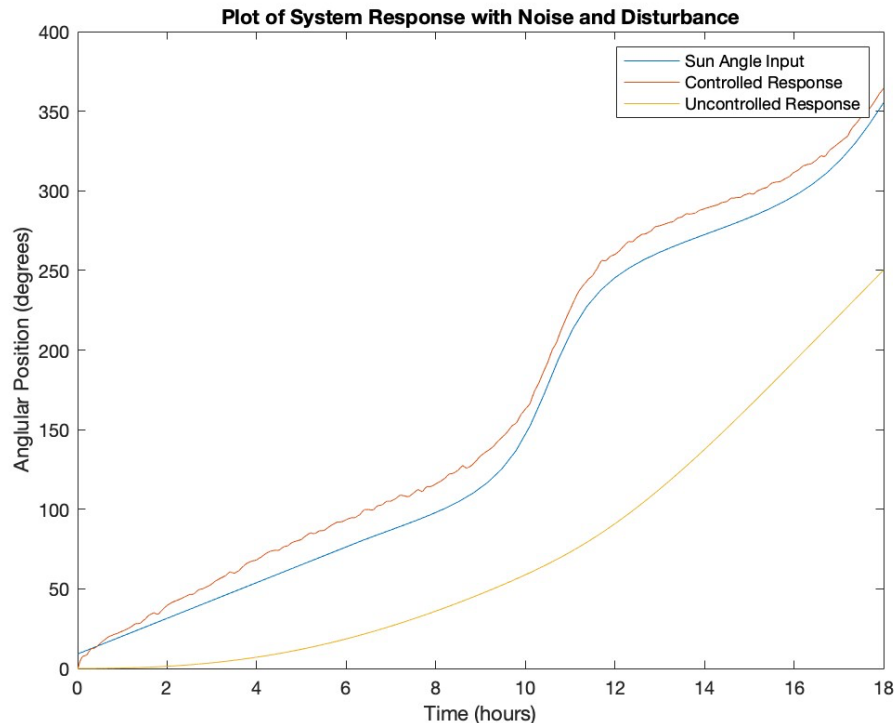


Figure 47: Controller Response with Noise and Disturbance.

Figure 47 illustrates that the solar tracker controller was able to operate efficiently even with disturbance and noise. The maximum error for the signal was 10 degrees which would still be suitable to capture sunlight from the sun effectively, though the solar panel itself may be offset a bit at some moments.

#### 4.4.1.1. Recommendations for dealing with Disturbances and Noise

- Implement low-pass filters to smooth out the sensor readings and reduce high-frequency noise from the potentiometer, as well as proper grounding of the wiring to minimize electrical noise and interference.
- Implement an adaptive control strategy where the PID controller parameters ( $K_p$ ,  $K_i$ ,  $K_d$ ) are adjusted in real-time based on wind conditions.
- Re-tune the PID controller
- Incorporate feedforward control in addition to the PID controller, which will anticipate disturbances such as predictable wind patterns and adjust the system proactively.

## 4.5. Discussion of controller performance

### 4.5.1. Control Accuracy and Precision

As shown earlier in ‘**section 4.2**’ the solar tracker PID controller has a zero steady state error. This means the controller is accurate at tracking the angle of the sun. The settling time for the final PID controller is 25.9 seconds which is suitable. This settling time is suitable as it avoids having a derivative kick where the system response is too fast due to the sudden change in the setpoint. The transient response of the system has a %overshoot of 7.61 which is small enough to allow the tracker to efficiently track the azimuth angle.

### 4.5.2. Responsiveness

The controller exhibits good responsiveness to input. The PID controller has a rise time of 2.62 seconds, and this exhibits a responsive behaviour, because it can capture any change in the sun’s angle quickly. Furthermore, this allows the solar tracker to operate effectively throughout the year as the seasons change.

### 4.5.3. Stability

The PID controlled system exhibits robustness with regards to stability as shown in ‘**section 4.3.2**’. The PID controller has a high tolerance for gain values. Thus it can operate with significantly high values before the system becomes unstable.

#### 4.5.4. Robustness

Due to the tuning of the PID controller, the system exhibits moderate robustness. The controller can handle small disturbances and noise without a large error. As the magnitude of the disturbance increases so does the error of the output signal. Thus, further compensation would be required to increase the robustness of the controller.

Thus the PID controller for the solar tracker is stable for large variations of gain, it is responsive without the derivative kick that rapidly changes the setpoint and it is moderately robust to noise and disturbance.

### 4.6. Discussion of instrumentation needed to fully implement controller

This section highlights the different instrumentation that would allow for the implementation of a solar tracking system. The components listed include an example of an off-the-shelf component and the cost of the instrumentation. This instrumentation accounts for the control system and does not include the plant which is a solar panel fitted with a slew drive gear system as shown in ‘**section 1**’.

#### 4.6.1. Micro Controller/ PLC

A micro controller or programmable logic controller is the main part of a control system. This part is considered the brain of the system which will allow control algorithm to be uploaded and applied to the system. An example of a micro controller is the Arduino-nano Compatible v3.0, which retails for R299 [17].



Figure 48: Micro Controller [17]

#### 4.6.2. Power Supply

Power supply is needed to allow for the actuation and control of the solar panel. This power supply can come in the form of a battery or AC power supply from the country's grid. The power supply is dependent on the size of the motor attached to the system.

#### 4.6.3. Potentiometer

A potentiometer is the sensor that allows the tracking and comparing of the sun's angle to the input angle of the motor. This potentiometer operates by converting the rotational position into a resistance. The limit the input voltage into the system. An example of a potentiometer is the 10 turn Precision Potentiometer which retails for R250 [18].



Figure 49: Potentiometer [18]

#### 4.6.4. DC Motor

A motor is required to actuate the plant (solar panel), this is to allow the panel to orientate and face the angle of the sun. A DC motor allows for better position control than an AC motor. A common DC motor is the permanent magnet DC brushless motor, which retails for R2000 [19].



Figure 50: Permanent Magnet DC Gear Motor [19]

#### 4.6.5. Comparator/Signal Amplifier

A comparator is the unit that compares two voltage signals and computes the difference between the two as an error signal. This allows the output signal to be compared to the input signal to allow for control of the system. A signal amplifier increases the intensity of the error signal. These two components are normally incorporated into one unit. An example of this unit is the Lm358 Operational Amplifier Adjustable which retail for R150 [20].

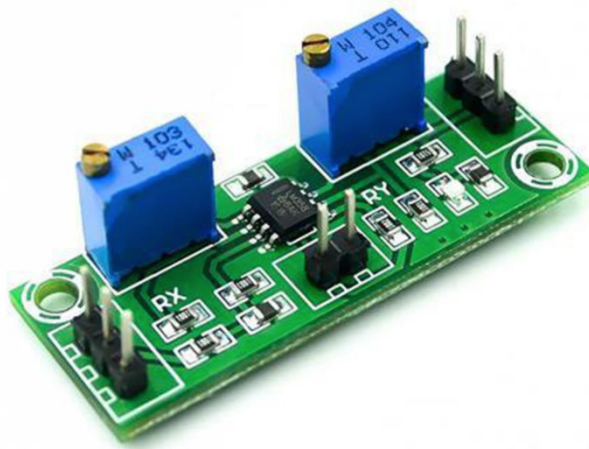


Figure 51: Signal Amplifier [20]

#### 4.6.6. Wi-Fi Module for monitoring

A Wi-Fi module is the part of the system that will allow for the tracking and monitoring of the system performance. This module allows the system to communicate with a computer to allow the mechatronics engineer to track the performance and the response of the system. A low cost Wi-Fi module retails for R180 [21].



Figure 52: Wi-Fi Module [21]

## REFERENCES

- [1] S. D. Hanwate and Y. V. Hote, ‘Design of PID controller for sun tracker system using QRAWCP approach’, *Int. J. Comput. Intell. Syst.*, vol. 11, no. 1, pp. 133–145, Jan. 2018, doi: 10.2991/ijcis.11.1.11.
- [2] ‘Solar Tracker System Specifications: Everything You Need to Know’. Accessed: Apr. 08, 2024. [Online]. Available: <https://vuphong.com/solar-tracker-system/>
- [3] ‘2024-03 - Rooftop projects boost clean energy - Wits University’. Accessed: May 20, 2024. [Online]. Available: <https://www.wits.ac.za/news/latest-news/general-news/2024/2024-03/rooftop-projects-boost-clean-energy.html>
- [4] ‘School of Mechanical, Industrial and Aeronautical Engineering, WITS · South West Engineering Building, First Floor, East Campus, Yale Road Braamfontein, 2050, Johannesburg, 2017’, School of Mechanical, Industrial and Aeronautical Engineering, WITS · South West Engineering Building, First Floor, East Campus, Yale Road Braamfontein, 2050, Johannesburg, 2017. Accessed: May 20, 2024. [Online]. Available: <https://www.google.com/maps/place/School+of+Mechanical,+Industrial+and+Aeronautical+Engineering,+WITS/@-26.1917981,28.0294,3334m/data=!3m1!1e3!4m6!3m5!1s0x1e950c05442d26bb:0x1426e46d74274be!8m2!3d-26.1917981!4d28.0294!16s%2Fg%2F11f3s82nlg?entry=ttu>
- [5] Latitude.to, ‘GPS coordinates of University of the Witwatersrand, South Africa. Latitude: -26.1878 Longitude: 28.0248’, Latitude.to, maps, geolocated articles, latitude longitude coordinate conversion. Accessed: Apr. 09, 2024. [Online]. Available: <http://latitude.to:8080/articles-by-country/za/south-africa/4705/university-of-the-witwatersrand>
- [6] P. E. Hertzog and A. J. Swart, ‘The impact of atmospheric conditions on the sustainability of a PV system in a semi-arid region: A case study from South Africa’, in *2016 13th International Conference on Electrical Engineering/Electronics, Computer, Telecommunications and Information Technology (ECTI-CON)*, Jun. 2016, pp. 1–6. doi: 10.1109/ECTICon.2016.7561267.
- [7] ‘Renewable Energy | Department: Energy | REPUBLIC OF SOUTH AFRICA’. Accessed: Apr. 09, 2024. [Online]. Available: [https://www.energy.gov.za/files/esources/renewables/r\\_solar.html](https://www.energy.gov.za/files/esources/renewables/r_solar.html)
- [8] J. MAIA *et al.*, *Green jobs: Estimating the employment potential of a growing green economy in South Africa*. 2011.
- [9] ‘Yonkers Public Schools / Homepage’. Accessed: May 20, 2024. [Online]. Available: <https://www.yonkerspublicschools.org/>
- [10] ‘Section 2.9 - MECN 4029A: Mechatronics II | zyBooks’. Accessed: Apr. 22, 2024. [Online]. Available: <https://learn.zybooks.com/zybook/ACMECN4029APandayWinter2024/chapter/2/section/9>

- [11] ‘List of moments of inertia’, *Wikipedia*. Apr. 29, 2024. Accessed: May 04, 2024. [Online]. Available: [https://en.wikipedia.org/w/index.php?title=List\\_of\\_moments\\_of\\_inertia&oldid=1221383172](https://en.wikipedia.org/w/index.php?title=List_of_moments_of_inertia&oldid=1221383172)
- [12] ‘Section 4.6 - MECN 4029A: Mechatronics II | zyBooks’. Accessed: May 15, 2024. [Online]. Available: <https://learn.zybooks.com/zybook/ACMECN4029APandayWinter2024/chapter/4/section/6>
- [13] ‘Section 6.2 - MECN 4029A: Mechatronics II | zyBooks’. Accessed: May 18, 2024. [Online]. Available: <https://learn.zybooks.com/zybook/ACMECN4029APandayWinter2024/chapter/6/section/2>
- [14] ‘Section 8.3 - MECN 4029A: Mechatronics II | zyBooks’. Accessed: May 20, 2024. [Online]. Available: <https://learn.zybooks.com/zybook/ACMECN4029APandayWinter2024/chapter/8/section/3>
- [15] ‘Basics of Positional Astronomy’. Accessed: May 20, 2024. [Online]. Available: <http://www.geoastro.de/sunpos/>
- [16] ‘Johannesburg, Gauteng, South Africa Hourly Weather | AccuWeather’. Accessed: May 20, 2024. [Online]. Available: <https://www.accuweather.com/en/za/johannesburg/305448/hourly-weather-forecast/305448>
- [17] ‘Robotico Arduino-compatible Nano v3.0 Atmega328P Development Board | Shop Today. Get it Tomorrow! | takealot.com’. Accessed: May 20, 2024. [Online]. Available: [https://www.takealot.com/robotico-arduino-compatible-nano-v3-0-atmega328p-development-boa/PLID91574265?gclsrc=aw.ds&gad\\_source=4&gclid=Cj0KCQjwxqayBhDFARIsAANWRnRtAbZK40ZKM49hRShEszQ8ob4rbk3L4z0dJ3Q0KxITQMLYnSnH3waAn3jEALw\\_wcB&gclsrc=aw.ds](https://www.takealot.com/robotico-arduino-compatible-nano-v3-0-atmega328p-development-boa/PLID91574265?gclsrc=aw.ds&gad_source=4&gclid=Cj0KCQjwxqayBhDFARIsAANWRnRtAbZK40ZKM49hRShEszQ8ob4rbk3L4z0dJ3Q0KxITQMLYnSnH3waAn3jEALw_wcB&gclsrc=aw.ds)
- [18] ‘10-Turn Precision Potentiometer - 3590S-2-103L | Shop Today. Get it Tomorrow! | takealot.com’. Accessed: May 20, 2024. [Online]. Available: [https://www.takealot.com/10-turn-precision-potentiometer-3590s-2-103l/PLID94738708?gclsrc=aw.ds&gad\\_source=1&gclid=Cj0KCQjwxqayBhDFARIsAANWRnQvJADiqjsCowOnCwI58jxeKX3sisxhh3ZlHe5sheUwl0F\\_em7k-XcaAubfEALw\\_wcB&gclsrc=aw.ds](https://www.takealot.com/10-turn-precision-potentiometer-3590s-2-103l/PLID94738708?gclsrc=aw.ds&gad_source=1&gclid=Cj0KCQjwxqayBhDFARIsAANWRnQvJADiqjsCowOnCwI58jxeKX3sisxhh3ZlHe5sheUwl0F_em7k-XcaAubfEALw_wcB&gclsrc=aw.ds)
- [19] ‘600W 750W 48V 60V Permanent Magnet DC Gear Motor, 2800 RPM Brushless Mid Motor for Electric Tricycle Application Light and Medium Duty Electric Tricycles (Color: 750w 60v) : Amazon.ca: Tools & Home Improvement’. Accessed: May 20, 2024. [Online]. Available: <https://www.amazon.ca/Permanent-Brushless-Electric-Application-Tricycles/dp/B0BVLW2XVH>
- [20] ‘Lm358 Operational Amplifier Adjustable | Shop Today. Get it Tomorrow! | takealot.com’. Accessed: May 20, 2024. [Online]. Available: [https://www.takealot.com/lm358-operational-amplifier-adjustable/PLID95199596?gclsrc=aw.ds&gad\\_source=1&gclid=Cj0KCQjwxqayBhDFARIsAANWRnTZh4NQWY5Ff\\_ISAA0mE2PrXkT1aM8xda8MpQYzu\\_tC2jWqsKnXgOUaAncfEALw\\_wcB&gclsrc=aw.ds](https://www.takealot.com/lm358-operational-amplifier-adjustable/PLID95199596?gclsrc=aw.ds&gad_source=1&gclid=Cj0KCQjwxqayBhDFARIsAANWRnTZh4NQWY5Ff_ISAA0mE2PrXkT1aM8xda8MpQYzu_tC2jWqsKnXgOUaAncfEALw_wcB&gclsrc=aw.ds)

- [21] ‘Low Cost Wi07c Wifi Module | Shop Today. Get it Tomorrow! | takealot.com’. Accessed: May 20, 2024. [Online]. Available: [https://www.takealot.com/low-cost-wi07c-wifi-module/PLID95180604?gclsrc=aw.ds&gad\\_source=1&gclid=Cj0KCQjwxqayBhDFARIsAANWRnRmsHWUZNBlgnJ2dkhkTrjgqgsLP4-LxQmZKIP2AUqwznmr1MWv3skaAr\\_DEALw\\_wcB&gclsrc=aw.ds](https://www.takealot.com/low-cost-wi07c-wifi-module/PLID95180604?gclsrc=aw.ds&gad_source=1&gclid=Cj0KCQjwxqayBhDFARIsAANWRnRmsHWUZNBlgnJ2dkhkTrjgqgsLP4-LxQmZKIP2AUqwznmr1MWv3skaAr_DEALw_wcB&gclsrc=aw.ds)

# APPENDICES

## A.1. MATLAB Codes

### A.1.1. Bode Plot – Uncontrolled

```
%% Transfer Function for Uncontrolled linear system

Num_1 = 112.93;
Den_1 = [1 2500 377 112.93]; % Coefficients from Denominator

Sys_1 = tf(Num_1, Den_1);

% Bode Plot
figure;
margin(Sys_1); % To indicate Gain and Phase margins on Bode Plot
```

### A.1.2. Bode Plot – PID Controlled

```
%% PID Controlled

Num_2 = [1.268e05 2.76e04 1479];
Den_2 = [1 2576 1.909e05 1.556e05 2.76e04 1479]; % Coefficients from Denominator

Sys_2 = tf(Num_2, Den_2);

% Bode Plot
figure;
margin(Sys_2); % To indicate Gain and Phase margins on Bode Plot
```

### A.1.3. Nyquist Plot – Uncontrolled

```
%% Uncontrolled
%% Transfer Function

Num_1 = 112.93;
Den_1 = [1 2500 377 112.93];
sys_1 = tf(Num_1, Den_1);

% The Nyquist plot
figure;
nyquist(sys_1);
title('Nyquist Plot');
grid on;

% Stability analysis using margins
[GM, PM] = margin(sys_1);

% Displaying Margins
disp('Gain Margin (dB):');
disp(20*log10(GM));
disp('Phase Margin (degrees):');
disp(PM);

% Comment on system's stability
if GM > 1 && PM > 0
    disp('The system is stable.');
else
    disp('The system is unstable.');
end
```

### A.1.4. Nyquist Plot – PID Controlled

```
%% PID Controlled
%% Transfer Function

Num_2 = [1.268e05 2.76e04 1479];
Den_2 = [1 2576 1.909e05 1.556e05 2.76e04 1479]; % Coefficients from Denominator

Sys_2 = tf(Num_2, Den_2);

% The Nyquist plot
figure;
nyquist(sys_2);
title('Nyquist Plot');
grid on;

% Stability analysis using margins
[GM, PM] = margin(sys_2);
```

```

        % Displaying Margins
disp('Gain Margin (dB):');
disp(20*log10(GM));
disp('Phase Margin (degrees):');
disp(PM);

        % Comment on system's stability
if GM > 1 && PM > 0
    disp('The system is stable.');
else
    disp('The system is unstable.');
end

```

### A.1.5. Pole Zero Plot – Uncontrolled

```

%% Uncontrolled
%Transfer Function
Num_1 = 112.93;
Den_1 = [1 2500 377 112.93];
sys_1 = tf(Num_1, Den_1);

%Pole-Zero plot
figure;
pzmap(sys_1);
title('Pole-Zero Plot');
grid on;

%Poles and Zeros
poles = pole(sys_1);
zeros = zero(sys_1);
hold on;

plot(real(poles), imag(poles), 'rx', 'MarkerSize', 10, 'LineWidth', 2);
plot(real(zeros), imag(zeros), 'bo', 'MarkerSize', 10, 'LineWidth', 2);
hold off;

% Stability Analysis
if all(real(poles) < 0)
    disp('The system is stable.');
elseif any(real(poles) == 0)
    disp('The system is marginally stable.');
else
    disp('The system is unstable.');
end

```

### A.1.6. Pole Zero Plot – PID Controlled

```

%% PID Controlled
%Transfer Function
Num_2 = [1.268e05 2.76e04 1479];
Den_2 = [1 2576 1.909e05 1.556e05 2.76e04 1479]; % Coefficients from Denominator
sys_2 = tf(Num_2, Den_2);

%Pole-Zero plot
figure;
pzmap(sys_2);
title('Pole-Zero Plot');
grid on;

%Poles and Zeros
poles = pole(sys_2);
zeros = zero(sys_2);
hold on;

plot(real(poles), imag(poles), 'rx', 'MarkerSize', 10, 'LineWidth', 2);
plot(real(zeros), imag(zeros), 'bo', 'MarkerSize', 10, 'LineWidth', 2);
hold off;

% Stability Analysis
if all(real(poles) < 0)
    disp('The system is stable.');
elseif any(real(poles) == 0)
    disp('The system is marginally stable.');
else
    disp('The system is unstable.');
end

```